Super-enhancer-driven expression of BAHCC1 promotes melanoma cell proliferation and genome stability

Pietro Berico, Maguelone Nogaret, Max Cigrang, Antonin Lallement, Fatemeh Vand-Rajabpour, Amanda Flores-Yanke, Giovanni Gambi, Guillaume Davidson, Leane Seno, Julian Obid, et al.

Cell Reports

Article

Super-enhancer-driven expression of BAHCC1 promotes melanoma cell proliferation and genome stability

Graphical abstract

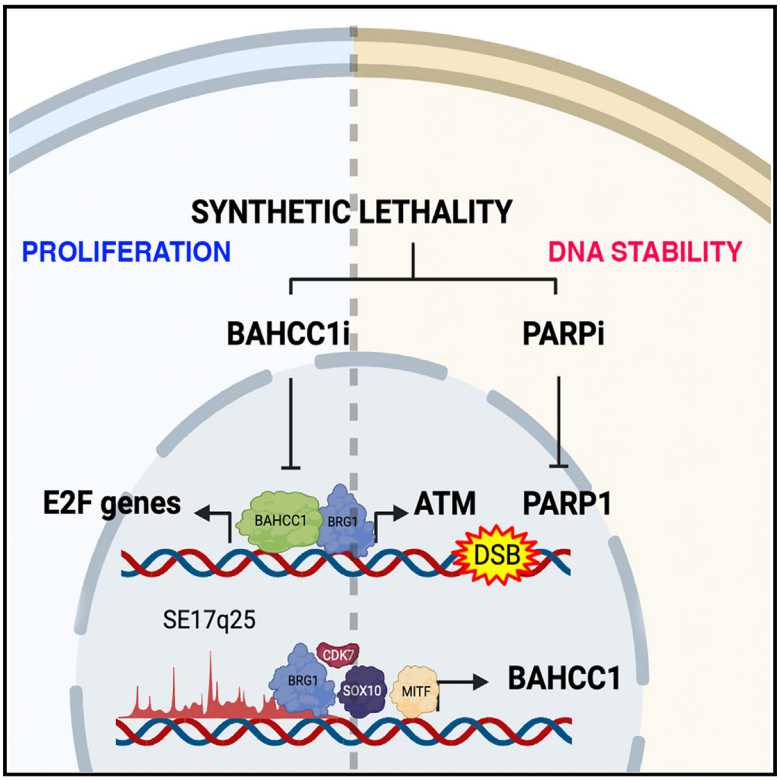

Highlights

- BAHCC1 is highly expressed in melanoma cells
- BAHCC1 regulates expression of DNA-repair and E2F/KLF-dependent cell-cycle genes
- BAHCC1 depletion impairs tumor engraftment, growth, and dissemination
- BAHCC1 deficiency cooperates with PARP inhibition to induce melanoma cell death

Authors

Pietro Berico, Maguelone Nogaret, Max Cigrang, ..., Eva Hernando, Irwin Davidson, Frédéric Coin

Correspondence

irwin@igbmc.fr (I.D.),
fredr@igbmc.fr (F.C.)

In brief

Berico et al. identify a MITF/SOX10/TFIIH-dependent super-enhancer promoting the expression of BAHCC1 in a broad panel of melanoma cells. Integrative genomics analyses reveal that BAHCC1 is a transcriptional regulator controlling expression of E2F/KLF-dependent cell-cycle and DNA-repair genes in melanoma.

Berico et al., 2023, Cell Reports *42*, 113363
November 28, 2023
https://doi.org/10.1016/j.celrep.2023.113363

CellPress

Cell Reports

CellPress
OPEN ACCESS

Article

Super-enhancer-driven expression of BAHCC1 promotes melanoma cell proliferation and genome stability

Pietro Berico,[1,2,3,4,7,8] Maguelone Nogaret,[1,2,3,4] Max Cigrang,[1,2,3,4] Antonin Lallement,[1,2,3,4] Fatemeh Vand-Rajabpour,[7,8] Amanda Flores-Yanke,[7,8] Giovanni Gambi,[1,2,3,4] Guillaume Davidson,[1,2,3,4] Leane Seno,[1,2,3,4] Julian Obid,[1,2,3,4] Bujamin H. Vokshi,[1,2,3,4] Stephanie Le Gras,[1,2,3,4] Gabrielle Mengus,[1,2,3,4] Tao Ye,[1,2,3,4] Carlos Fernandez Cordero,[7,8] Mélanie Dalmasso,[5,6] Emmanuel Compe,[1,2,3,4] Corine Bertolotto,[5,6] Eva Hernando,[7,8] Irwin Davidson,[1,2,3,4,*] and Frédéric Coin[1,2,3,4,9,*]

[1]Institut de Génétique et de Biologie Moléculaire et Cellulaire, Equipe Labéllisée, "Ligue contre le Cancer 2022", BP 163, 67404 Illkirch Cedex, C.U. Strasbourg, France
[2]Centre National de la Recherche Scientifique, UMR7104, 67404 Illkirch, France
[3]Institut National de la Santé et de la Recherche Médicale, U1258, 67404 Illkirch, France
[4]Université de Strasbourg, 67404 Illkirch, France
[5]Université Côte d'Azur, Nice, France
[6]INSERM, Biology and Pathologies of Melanocytes, Equipe labellisée "Ligue contre le Cancer 2020" and Equipe labellisée "Fondation ARC 2022", Centre Méditerranéen de Médecine Moléculaire, Nice, France
[7]Department of Pathology, New York University Grossman School of Medicine, New York, NY 10016, USA
[8]Interdisciplinary Melanoma Cooperative Group, Perlmutter Cancer Center, NYU Langone Health, New York, NY 10016, USA
[9]Lead contact
*Correspondence: irwin@igbmc.fr (I.D.), fredr@igbmc.fr (F.C.)
https://doi.org/10.1016/j.celrep.2023.113363

SUMMARY

Super-enhancers (SEs) are stretches of enhancers ensuring a high level of expression of key genes associated with cell function. The identification of cancer-specific SE-driven genes is a powerful means for the development of innovative therapeutic strategies. Here, we identify a MITF/SOX10/TFIIH-dependent SE promoting the expression of BAHCC1 in a broad panel of melanoma cells. BAHCC1 is highly expressed in metastatic melanoma and is required for tumor engraftment, growth, and dissemination. Integrative genomics analyses reveal that BAHCC1 is a transcriptional regulator controlling expression of E2F/KLF-dependent cell-cycle and DNA-repair genes. BAHCC1 associates with BRG1-containing remodeling complexes at the promoters of these genes. BAHCC1 silencing leads to decreased cell proliferation and delayed DNA repair. Consequently, BAHCC1 deficiency cooperates with PARP inhibition to induce melanoma cell death. Our study identifies BAHCC1 as an SE-driven gene expressed in melanoma and demonstrates how its inhibition can be exploited as a therapeutic target.

INTRODUCTION

Transcriptional deregulation represents a key mechanism for cancer initiation and progression.[1] A combination of somatic mutations and microenvironmental cues leads to the overexpression of transcription regulators promoting aberrant gene expression programs, ultimately resulting in cancer hallmarks.[2] A key mechanism promoting tumor-specific gene expression programs is the aberrant activation of super-enhancers (SEs), broad gene regulatory elements highly dependent on the activity of general co-activators compared to canonical enhancers.[3] Consequently, transcriptional inhibitors targeting co-activators such as BRD4 (bromodomain-containing protein 4) and the cyclin-dependent kinase 7 (CDK7) of the basal transcription factor TFIIH are widely used to disrupt SE-associated genes in cancer cells.[4,5] However, the presence of SE-associated genes in healthy cells, together with the poor pharmacokinetics and efficacy of transcriptional inhibitors in human clinical trials, underscores the need for alternative strategies[6,7] such as the identification of cancer-specific SE-driven genes.[8]

Cutaneous melanoma remains the most lethal skin cancer, with an incidence that has continued to increase over the past few decades.[9,10] Despite the significant improvement in 5-year overall survival provided by therapies targeting mitogen-activated protein kinase (MAPK) including vemurafenib and trametinib (BRAF and MEK inhibitors, respectively),[11,12] or by immune checkpoint inhibitors anti-PD1 and anti-CTLA4,[13] many patients still develop resistance, in part due to melanoma phenotypic plasticity, a dynamic and non-mutational mechanism of adaptation to microenvironmental changes and drug exposure.[14,15] Plasticity results in an important intratumor heterogeneity involving multiple cell states with distinct transcriptional

signatures and different proliferative, invasive, and drug-resistance phenotypes. Melanoma phenotype plasticity depends in part on two opposing gene expression programs, governed by the transcription factors MITF (microphthalmia-associated transcription factor) and SOX10 (SRY-box transcription factor 10) or AP-1 (activating protein 1) and TEAD (transcriptional enhancer associate domain), respectively, whose activities modulate melanoma cell-state transition.[16–19] Other forms of melanoma include uveal melanoma, the most common primary intraocular tumor in adults that is intrinsically different from cutaneous melanoma. In uveal melanoma, the most frequent driver mutations are those involving the heterotrimeric G-protein subunits GNAQ or GNA11.[20,21] Despite successful treatment of primary uveal melanoma, 50% of patients will develop metastases that are highly refractory to existing treatments.[22] Therefore, there is an urgent need to better understand the molecular mechanisms involved in these two cancers in order to develop efficient treatments.

Here, by using the global molecular features of SEs (enrichment in TFIIH/CDK7, BRG1, and H3K27ac) as well as those specific to melanoma cells (enrichment in MITF and SOX10), we characterized the SE landscapes of patient-derived short-term cutaneous melanoma cultures. Integrative epigenomic analyses revealed a melanoma-specific SE regulating the expression of the bromo-adjacent homology and coiled-coil domain-containing 1 (BAHCC1) protein in a broad panel of cutaneous, but also uveal, melanoma cells. BAHCC1 drives cutaneous and uveal melanoma cell proliferation and is required for tumor growth and engraftment of cutaneous melanoma cells *in vivo*. Loss-of-function and genomic profiling experiments show that BAHCC1 is a transcriptional regulator controlling the expression of a subset of E2F (E2 factor)/KLF (Krüppel-like factor)-dependent cell-cycle and DNA-repair genes in melanoma cells. BAHCC1 associates with BRG1 (BRM/SWI2-related gene 1)-containing remodeling complexes at the promoters of these genes. Consistent with the involvement of BAHCC1 in the regulation of DNA-repair genes, including the crucial cell-cycle kinase ATM (ataxia telangiectasia mutated), BAHCC1 depletion delays DNA repair and cooperates with PARP (poly ADP-ribose polymerase) inhibition to induce melanoma cell death. We thus identify BAHCC1 as an SE-dependent pan-melanoma expressed gene and demonstrate how its inhibition can be leveraged to impair melanoma cell proliferation, alone or in combination with DNA-damage-inducing agents.

RESULTS

SE17q25 regulates BAHCC1 expression in melanoma

To identify skin cutaneous melanoma (SKCM)-specific SEs, we performed *in silico* rank ordering of SE (ROSE)[23] analysis of H3K27ac chromatin immunoprecipitation sequencing (ChIP-seq) data from short-term melanoma cultures (MM)[16] and two normal human melanocyte (NHEM) samples (NHEM1 and -2).[8] The MM panel covered the two main phenotypes and most common driver mutations (Table S1). We further ranked SEs using DiffBind according to the enrichment in the binding of the lineage-specific transcription factors MITF and SOX10, which are recruited to long and short enhancers in melanocytic-like melanoma cells (Figure S1A).[24–27] Using these criteria, we identified a collection of potential SEs active in MM cells (Table S2). We further defined *bona fide* melanoma-specific SEs as active in at least 5 MM cell cultures. An SE at chr17q25.3 (hereafter referred to as SE17q25) met these criteria and was absent from NHEMs (Figures 1A, left, and S1B). The SE17q25 region measured around 20 kb and was recurrent not only in many of the MM cells but also in melanoma cell lines such as SK-MEL-5 and 501mel (Figure 1A, left and right; Table S2).

SE17q25 localized in close proximity to the promoter of the protein-coding gene BAHCC1 (Figure 1A). The Cancer Genome Atlas (TCGA) reports that high SE17q25 activity, as measured by the level of ATAC (assay for transposase-accessible chromatin)-seq signal, correlated with high BAHCC1 expression in several tumors and that the highest SE17q25 activity was observed in SKCM, with the highest BAHCC1 expression (Figure 1B). qRT-PCR and western blotting showed that BAHCC1 displayed higher RNA and protein levels in melanoma cells highly expressing MITF and SOX10, including melanocytic-like melanoma cells (501mel, MM117, IGR-37, SK-MEL-28, SK-MEL-5, MM011) and uveal melanoma (UVM) cells (OMM1, OMM1.3, OMM2.5) (Figures S1C and S1D). In agreement with these observations, analyses of the Cancer Cell Line Encyclopedia (CCLE) revealed that BAHCC1 expression correlated with that of MITF in melanoma cell lines (n = 49) (Figure 1C). Furthermore, depletion of SOX10 or MITF strongly reduced BAHCC1 mRNA and protein expression in melanocytic-like melanoma cells (Figures 1D and 1E). Note that MITF depletion reduced BRG1 recruitment at SE17q25, suggesting the decommission of this SE (Figure S1E).

Compared to melanocytic-like melanoma cells, BAHCC1 was less expressed in mesenchymal-like MITF^{LOW} melanoma cells (MM099, MM047, IGR-39, and MM029) (Figures S1C and S1D). Note, however, that BAHCC1 expression remained significantly higher in MITF/SOX10^{LOW} melanoma cells compared to non-transformed (but immortalized) Hermes3A melanocytes or the non-melanoma cell line U-2 OS (Figure S1D), arguing that activation of SE17q25 and BAHCC1 expression therefore requires not only MITF/SOX10 expression but additional events that accompany oncogenic transformation.

In addition to MITF and SOX10, the ATP-dependent chromatin remodeler BRG1 and the TFIIH kinase CDK7, which is known to associate with SEs,[28] also bound SE17q25 in 501mel cells (Figure 1A, right). Interestingly, treatment of 501mel cells for a short period of time with TFIIH inhibitors (the CDK7 inhibitor THZ1[5] or the TFIIH/XPB inhibitor triptolide[29,30]) significantly diminished BAHCC1 expression (Figure 1F). In parallel, CRISPR interference (CRISPRi) of SE17q25 in 501mel using a dead Cas9 (dCas9) fused with the repressive Krüppel-associated box (KRAB) domain (dCas9^{KRAB}) and guide RNAs targeting SE17q25 (gSE17q25) diminished BAHCC1 expression compared to GAPDH control gene (Figure 1G). Altogether these data link SE17q25 activity to BAHCC1 expression in melanoma cells.

BAHCC1 expression increases during melanoma progression

To explore BAHCC1 expression in tumors, we analyzed public transcriptional data and observed first that BAHCC1 was more strongly expressed in melanoma cell lines compared to other

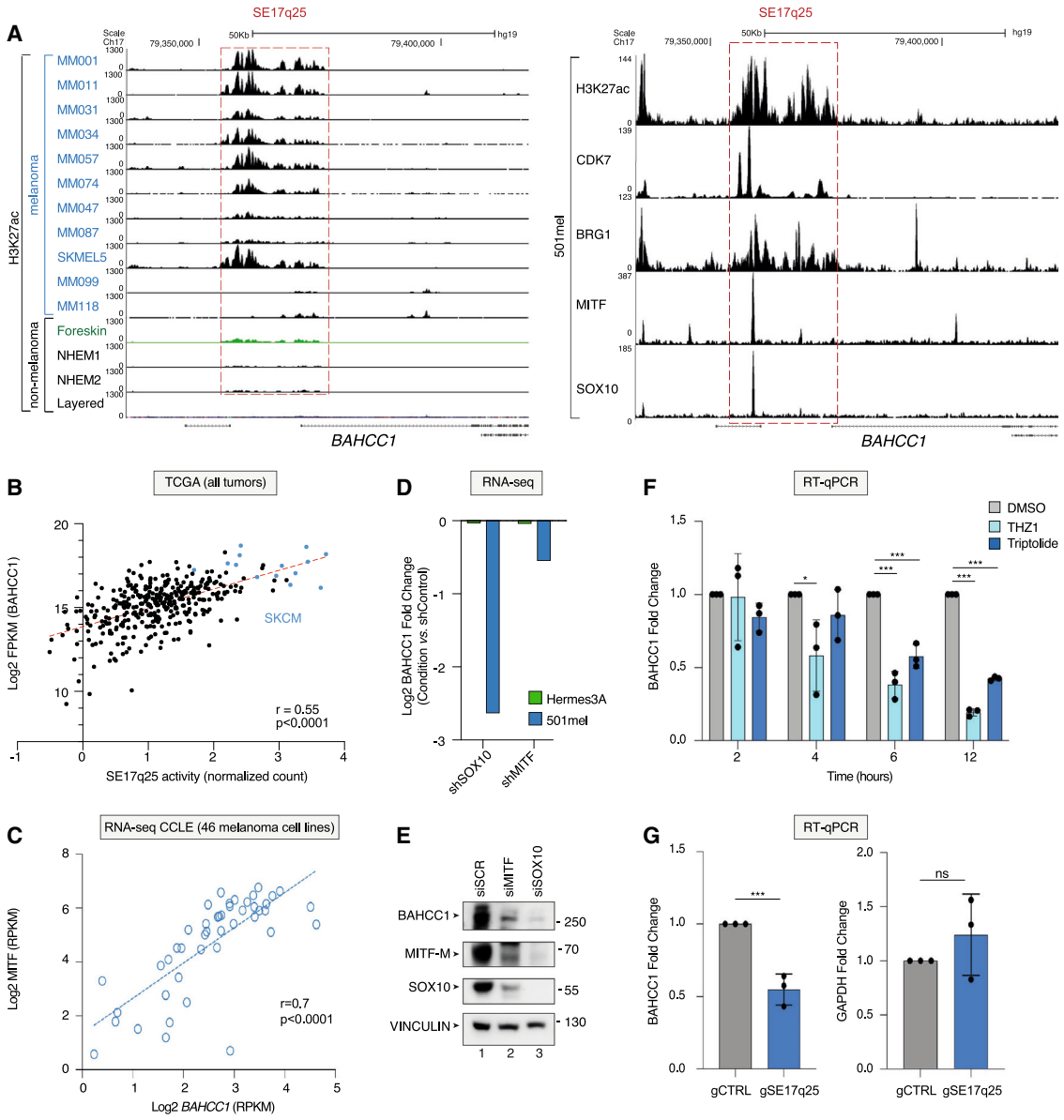

Figure 1. SE17q25 regulates BAHCC1 expression in melanoma

(A) Left: captures of the UCSC genome browser (GRCh38/hg19) showing the ChIP-seq profiles of H3K27ac in the genomic region of SE17q25 in several MM cell lines, healthy melanocytes (NHEM, normal human epidermal melanocytes; foreskin, human foreskin melanocytes) and other tumor and healthy cell lines (layered: H3K27ac mark on 7 cell lines from ENCODE project). Right: captures of the UCSC genome browser (GRCh38/hg19) showing the ChIP-seq profiles of H3K27ac, CDK7, BRG1, MITF, and SOX10 at SE17q25 in mel501 cells. RefSeq-annotated genes are displayed at the bottom.

(B) Spearman correlation between BAHCC1 RNA expression and SE17q25 activity, as defined by the ATAC-seq signal (normalized count), measured in different TCGA tumor samples (n = 399). The SKCM samples are highlighted in light blue and have the higher expression of BAHCC1 and SE17q25 activity. "Spearman r" and p value are shown on bottom right.

(C) Dot plot of BAHCC1 vs. MITF expression (RPKM) determined by RNA-seq from melanoma cell lines obtained from the CCLE datasets (n = 49). The linear regression curve is shown in blue. "Spearman r" and p value are shown on bottom right.

(D) BAHCC1 mRNA fold change (condition vs. shControl) upon SOX10 or MITF KD in healthy melanocytes (Hermes3A) or 501mel melanoma cells obtained from GEO: GSE61967.

(E) 501mel melanoma cells were transfected with siSCR, siMITF, and siSOX10 for 24 h. Total extracts were resolved by SDS-PAGE and immunoblotted against proteins as indicated. Molecular sizes are indicated.

(F) 501mel cells were treated with DMSO, THZ1, or triptolide for 2, 4, 6, and 12 h as indicated, and the relative amount of BAHCC1 mRNA was quantified by qRT-PCR. Bars represent mean values of three different experiments (biological triplicates) (±SEM), two-way ANOVA Šídák's multiple comparisons test.

(G) qRT-PCR for GAPDH and BAHCC1 in 501mel cells co-transfected with CRISPR-dCas9^{KRAB} and guide RNAs (gRNAs) against SE17q25 (gSE17q25) or a non-targeting genomic region (gCTRL). Bars represent mean values of three different experiments (biological triplicates) (±SEM); paired t test.

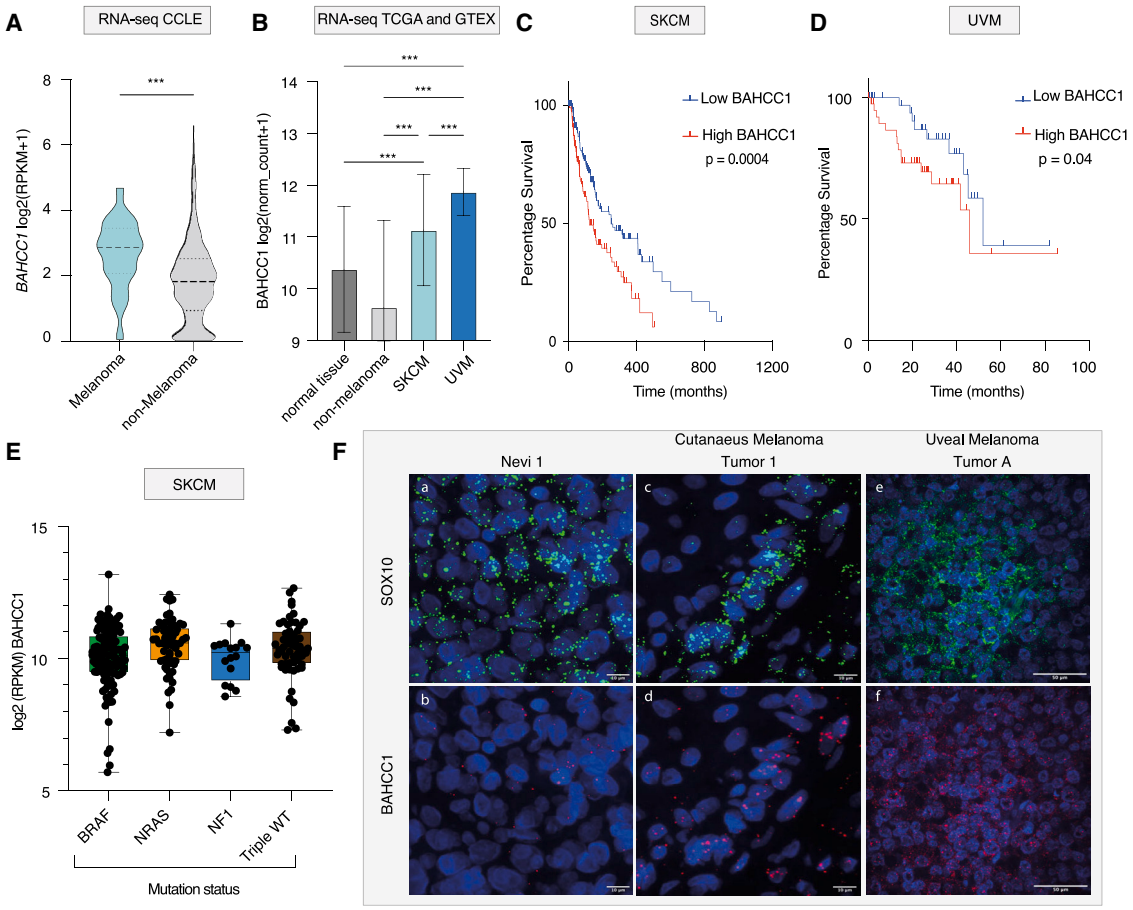

Figure 2. BAHCC1 is overexpressed in melanoma

(A) Violin plot of BAHCC1 levels in melanoma vs. non-melanoma cell lines (RPKM) obtained from CCLE (n = 1019); unpaired t test.

(B) Normalized RNA levels of BAHCC1 in healthy tissues (n = 8,156), non-melanoma tumors (n = 10,416), SKCM (n = 469), and UVM (n = 79) obtained from TCGA and The Genotype-Tissue Expression (GTEX) datasets. Ordinary one-way ANOVA using Dunnett's multiple comparisons test vs. all.

(C and D). Kaplan-Meier analysis of TCGA data from patients with SKCM (n = 302) (C) or UVM (n = 80) (D) with high or low BAHCC1 expression (lower and upper percentiles = 50); log-rank Mantel-Cox test.

(E) Box and whisker plot representation of BAHCC1 expression (RPKM) in TCGA data from patients with SKCM (n = 469) according to the BRAF, NRAS, and NF1 mutational status. Bars show the min and max values; box represent mean ± SEM.

(F) RNA fluorescence *in situ* hybridization (FISH) against BAHCC1 and SOX10 mRNA in naevus melanoma, cutaneous melanoma, and UVM tissue biopsies. Scale bars are indicated. Additional samples are shown in Figures S2E and S2F.

tumor cells (Figure 2A). In agreement, SKCM and UVM tumors from TCGA displayed higher levels of BAHCC1 compared to other tumors and healthy tissues (Figure 2B). Furthermore, BAHCC1 overexpression was a marker of poor prognosis in patients with SKCM or UVM (Figures 2C and 2D), and its expression was independent from the *BRAF*, *NRAS*, or *NF1* mutation status in patients with SKCM (Figure 2E).

To trace the evolution of BAHCC1 expression along melanoma initiation and progression, different published bulk and single-cell transcriptomic datasets from healthy cells and pre-malignant and malignant lesions were combined. Notably, we observed that BAHCC1 expression progressively increased going from healthy skin to primary melanoma and metastatic lesions specifically in malignant cells (Figures S2A–S2E) and that BAHCC1 levels were elevated in melanoma cells vs. melanocyte stem cells in BRAF mouse melanoma model (Figure S2F).[31] Using RNA *in situ* hybridization on a cohort of patient samples including benign nevi, cutaneous melanoma, and UVM, we confirmed the increased expression of BAHCC1 mRNA in SOX10-positive malignant cells (Figures 2F, S2G, and S2H). Overall, these results indicate that BAHCC1 expression progressively increases during melanoma progression from primary tumors to metastasis.

BAHCC1 is required for melanoma cell proliferation and tumor growth

To investigate the functional consequences of BAHCC1 knockdown (BAHCC1 KD), we transfected melanoma cells with two independent custom antisense oligonucleotides (ASOs; locked nucleic acid GapmeRs) targeting the BAHCC1 pre-mRNA ($GR^{\#1}$ and $GR^{\#2}$), which efficiently silenced BAHCC1 expression in 501mel cells (Figure S3A). BAHCC1 KD reduced

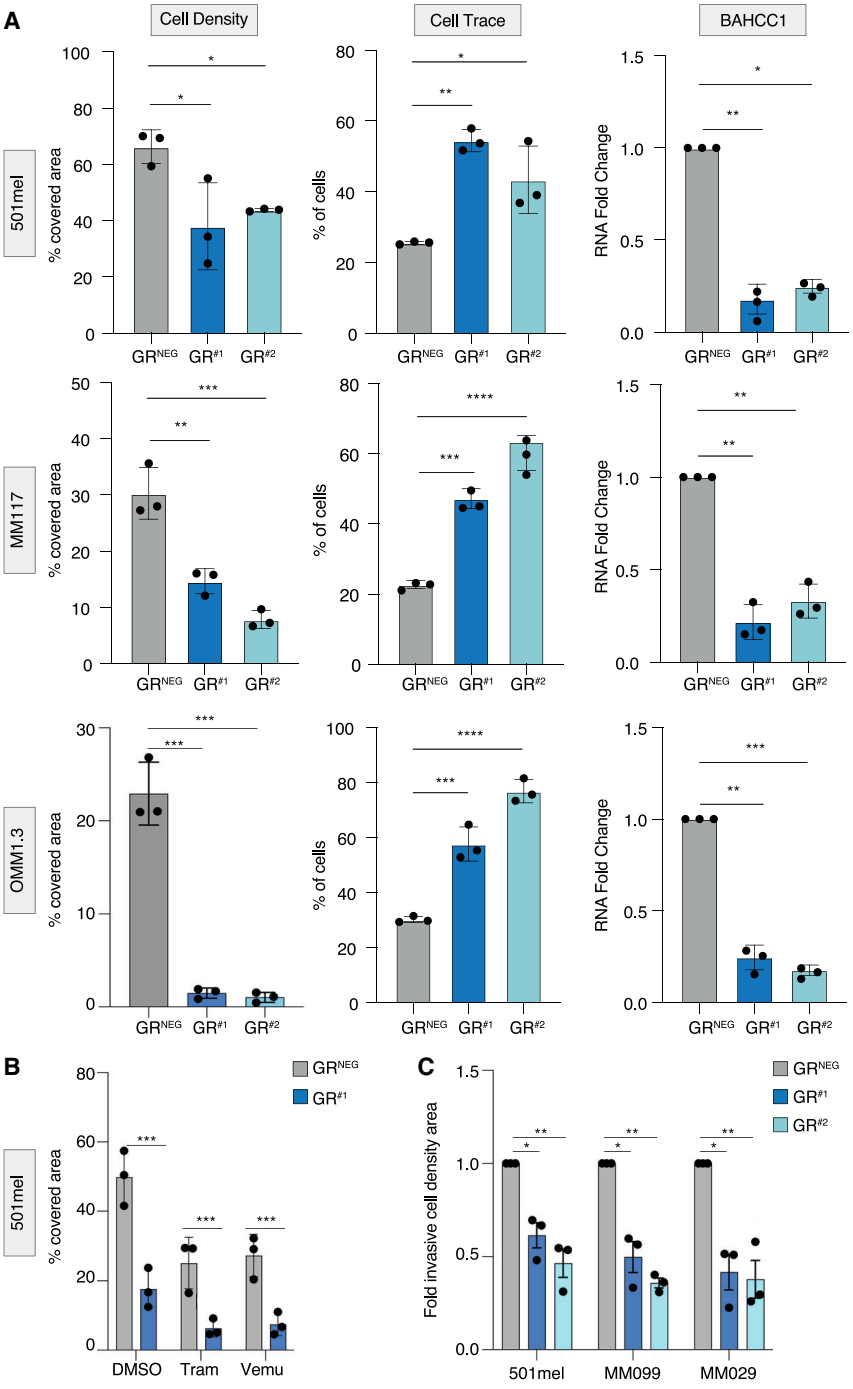

Figure 3. BAHCC1 depletion impairs melanoma cell proliferation

(A) Left: quantification of crystal violet staining of cells transfected with GapmeR^{NEG} (GR^{NEG}), GapmeR$^{\#1}$ (GR$^{\#1}$), and GapmeR$^{\#2}$ (GR$^{\#2}$) in SKCM cells (501mel and MM117) and UVM (OMM1.3) cells. Middle: CellTrace staining was measured by fluorescence-activated cell sorting (FACS) in the cells used on the left, and results are represented as a percentage of slow proliferative cells considering an arbitrary threshold between 20% and 30% in the GR^{NEG} control. Right: relative BAHCC1 expression upon transfection with GR^{NEG}, GR$^{\#1}$, and GR$^{\#2}$ were measured by qRT-PCR in the cells used on the left. Bars represent mean values of three different experiments (biological triplicates) (±SEM). Ordinary one-way ANOVA using Dunnett's multiple comparisons test.

(B) Cell coverage quantification of crystal violet staining of 501mel cells transfected with GR^{NEG} or GR$^{\#1}$ upon treatment with DMSO, trametinib (10 nM), or vemurafenib (5 μM). Bars represent mean values of three different experiments (biological triplicates) (±SEM). Ordinary one-way ANOVA using Dunnett's multiple comparisons test.

(C) Cell coverage quantification of the Boyden chamber Transwell after crystal violet staining of 501mel, MM099, and MM029 cells transfected with GR^{NEG}, GR$^{\#1}$, and GR$^{\#2}$. Bars represent mean values of three different experiments (biological triplicates) (±SEM). Two-way ANOVA using Tukey's multiple comparisons test.

proliferation of cutaneous melanocytic-like (501mel and MM117) and mesenchymal-like (MM047 and MM029) melanoma cells and also of UVM cell lines (OMM1.3 and OMM2.5) (Figures 3A and S3B). In contrast, BAHCC1 KD did not affect proliferation of U-2 OS cells excluding an off-target effect (Figure S3B). Given the anti-proliferative role of MAPK inhibitors (MAPKis) used in the clinic, we investigated whether BAHCC1 KD could exacerbate their effect. Indeed, BAHCC1 KD further reduced the proliferation of a melanocytic cell line upon treatment with trametinib or vemurafenib (Figure 3B). We also evaluated the effect of BAHCC1 KD on melanoma cell invasive capacity and observed that BAHCC1 KD significantly impaired migration of 501mel, MM099, and MM029 melanoma cells (Figure 3C). Altogether, these results highlight the importance of BAHCC1 for melanoma cell proliferation and invasion *in vitro*.

To test the effects of BAHCC1 silencing *in vivo*, we injected melanocytic 501mel melanoma cells engineered to constitutively express luciferase together with GFP and either a non-targeting short hairpin RNA (shRNA; SH^{NTC}) or two independent shRNAs against BAHCC1 (SH$^{\#1}$ and SH$^{\#2}$) in immunocompromised mice (Figure S4A). KD of BAHCC1 dramatically prevented cell-line-derived xenograft (CDX) tumor engraftment and growth compared to the SH^{NTC} (Figures 4A and 4B). In parallel, we also performed intracardiac injection of the 501mel cells to evaluate their capacity to disseminate and form lesions with or without BAHCC1 KD. Concordant with the *in vitro* proliferation and invasion assays, BAHCC1 KD completely prevented colonization in several organs, including the liver, as shown by bioluminescence and immunohistochemistry (IHC) (Figures 4C, 4D, and

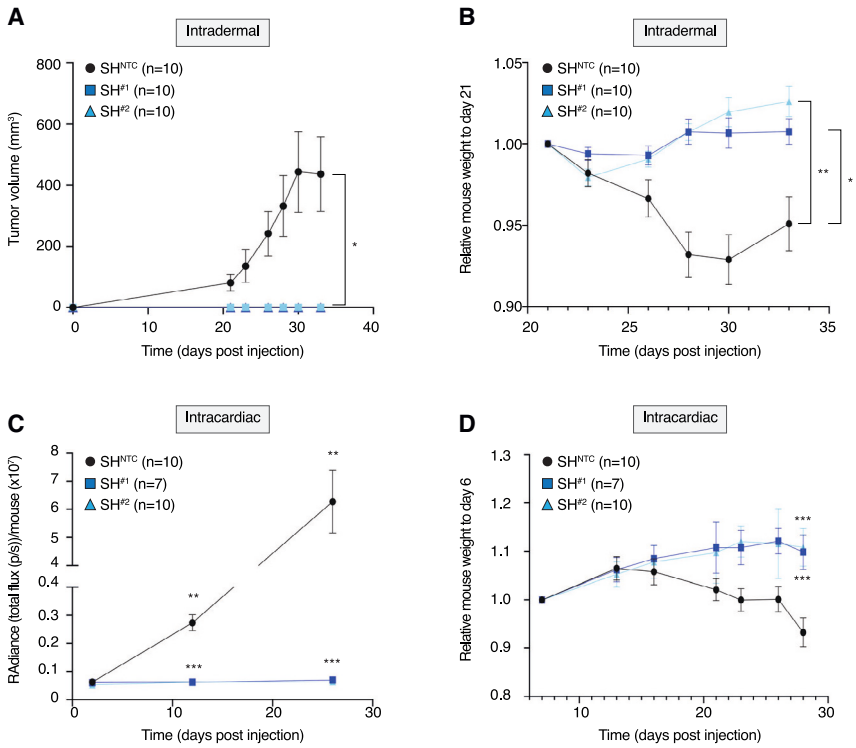

Figure 4. BAHCC1 depletion impairs melanoma tumor engraftment and metastatic growth

(A) Kinetics of tumor growth of 501mel melanoma cells stably expressing shNTC (SH^{NTC}) or shBAHCC1 ($SH^{\#1}$ and $SH^{\#2}$) injected intradermally in NSG mice (±SEM); number of mice per group are shown. Two-way ANOVA Dunnet's multiple comparisons test.

(B) Relative weights of mice after intracardiac injection of 501mel melanoma cells stably expressing SH^{NTC} or shBAHCC1 ($SH^{\#1}$ and $SH^{\#2}$), measured every 3 days after day 21 post-injection. Each mouse weight was normalized to day 21 weight. Two-way ANOVA Dunnet's multiple comparisons test.

(C) Bioluminescence was measured in the three intracardiac groups as indicated at days 2, 12, and 26 post-injection. Bioluminescence is expressed as total radiance per mouse. Number of animals per group are displayed. Two-way ANOVA Dunnet's multiple comparisons test.

(D) Animal weights were measured as indicated at days 7, 13, 16, 21, 23, 26, and 28 post-injection. Weight was scaled to day 7 for each mouse to evaluate the relative variations. Two-way ANOVA Dunnet's multiple comparisons test.

S4B–SD). These data demonstrate the critical role of BAHCC1 in melanoma tumor engraftment and growth *in vivo*.

BAHCC1 regulates E2F/KLF target genes involved in DNA repair and cell cycle

To better understand BAHCC1 function in melanoma cell proliferation, we first checked its localization by immunofluorescence in 501mel cells and observed its nuclear localization (Figure S5A). Analysis of subcellular protein fractions by immunoblot confirmed BAHCC1 accumulation in the nuclear soluble and insoluble fractions (Figure S5B). We then investigated the potential role of BAHCC1 to regulate melanoma gene expression first by transcriptome profiling of 501mel and MM047 cells before and after BAHCC1 KD. RNA-seq revealed that several hundred genes were deregulated in the absence of BAHCC1 (absolute log2 fold change > 0.5 and adjusted p value < 0.05) (Figure 5A), with a significant overlap of 200 genes between the 501mel and MM047 cells (Figure 5B; Table S3). Gene Ontology (GO) analyses of the 200 co-downregulated and 82 co-upregulated genes revealed their enrichment in cell cycle (MCM7, TOP2A, CNTRL), DNA repair (RAD51B, FANCG, ATM), and regulation of the MAPK pathway (MAP2K1, CDKN1B, CDKN2C), as well as mitochondria biogenesis (MTFR1, IMMP2L, DNA2) and cell migration (MMP2, COL18A1, BMP1) (Figures 5C and S5C), consistent with the anti-proliferative and anti-invasive effects of BAHCC1 KD observed above. Note that no modification of the melanocytic signature of 501mel nor the mesenchymal signature of MM047 was observed after BAHCC1 KD (Figure S5D).

To evaluate if BAHCC1 directly regulates gene expression by chromatin binding, we profiled endogenous BAHCC1 ($BAHCC1^{WT}$ [wild type]) genome-wide occupancy using CUT&Tag followed by deep sequencing in 501mel cells. We identified 31,280 peaks for endogenous $BAHCC1^{WT}$, localizing mostly in proximal gene promoters (37.62%) and distal intergenic (24.28%) regions (Figure S5E). Read density clustering of $BAHCC1^{WT}$, H3K27ac ChIP-seq, and ATAC-seq in the 31,280 BAHCC1-occupied regions demonstrated that $BAHCC1^{WT}$ mostly binds to active chromatin at the nucleosome-depleted regions between two H3K27ac-marked nucleosomes (Figure 5D). Moreover, a large fraction of the 41,088 annotated transcription start sites (TSSs) showed TSS-centered BAHCC1 and ATAC peaks flanked by H3K27ac chromatin marks (Figure 5E). Consistent with these data, analysis of the 1,000 best-scoring BAHCC1-occupied sites with RSAT to identify transcription factor DNA-binding motifs and transcription factors that may cooperate with or recruit BAHCC1 to regulate gene expression revealed strong enrichment of the NFY- and SP-family factors known to be enriched at proximal promoters (Table S4). Integrating BAHCC1 RNA-seq and CUT&Tag data, we observed that among the 11,385 genes associated with TSS-centered BAHCC1 peaks, 783 genes were deregulated upon BAHCC1 KD in 501mel cells, of which 539 (70%) were downregulated and 244 (30%) were upregulated (Figure 5F). RSAT analyses of the DNA motifs under the BAHCC1-bound sites at the downregulated promoters showed enrichment of NFY as above but also of motifs for KLF-family factors. Analyses of the promoters of upregulated genes showed KLF-family factors but also SOX10 (Table S4).

Further evidence for the role of BAHCC1 in cell-cycle gene regulation came from mining of single-cell RNA-seq (scRNA-seq)

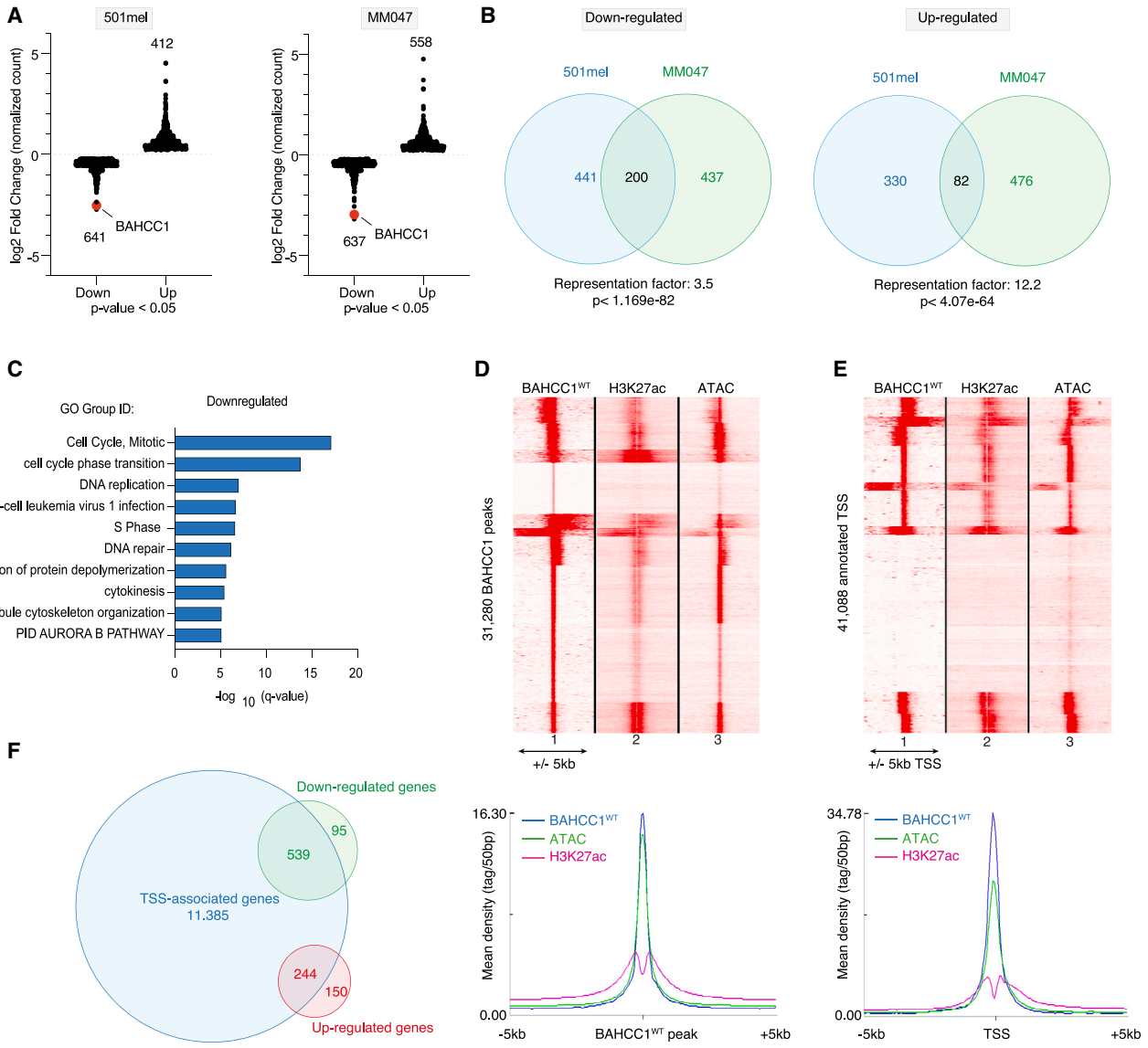

Figure 5. BAHCC1 is a transcriptional regulator

(A) Scatterplot of the significantly ($p < 0.05$) deregulated genes (normalized count) upon BAHCC1 KD in 501mel and MM047. Red dots highlight BAHCC1, which is one of the top downregulated genes.

(B) Venn diagram between significantly downregulated (top) and upregulated (bottom) genes identified by RNA-seq in 501mel and MM047 upon BAHCC1 KD. Representation factor and p values were calculated using hypergeometric test.

(C) GO analysis of the 200 co-downregulated genes between 501mel and MM047 upon BAHCC1 KD. The 10 most significant annotation groups are listed from top to bottom according to the −log10(q value).

(D) Top: read density clustering obtained with seqMINER for the 31,280 BAHCC1-occupied sites relative to BAHCC1, H3K27ac, and ATAC-seq signals in 501mel cells in a genomic window of 10 kb around the peaks. Bottom: merge meta-profile distribution of BAHCC1, H3K27ac, and ATAC enrichment relative to the 31,280 BAHCC1 peaks.

(E) Top: read density clustering obtained with seqMINER for BAHCC1, H3K27ac, and ATAC-seq signals relative to the 41,088 annotated TSSs. Bottom: merge meta-profile distribution of BAHCC1, H3K27ac, and ATAC in a ±5 kb window around the TSS.

(F) Venn diagram between genes showing a TSS-associated BAHCC1 protein and the significantly down- or upregulated genes following BAHCC1 KD, as determined by RNA-seq.

from melanoma patient-derived xenografts (PDXs)[17,26] where BAHCC1 seemed to be preferentially expressed in the "mitotic" melanoma cell subpopulation (Figure S5F) that was also significantly enriched in E2F and SP/KLF regulons (Figure S5G). Similarly, scRNA-seq from uveal and cutaneous tumors[32,33] were separated into "slow"- or "fast"-cycling cells according to the Tirosh cell-cycle signature (95 genes) (Table S5). We observed that BAHCC1 was significantly enriched in fast-cycling cells

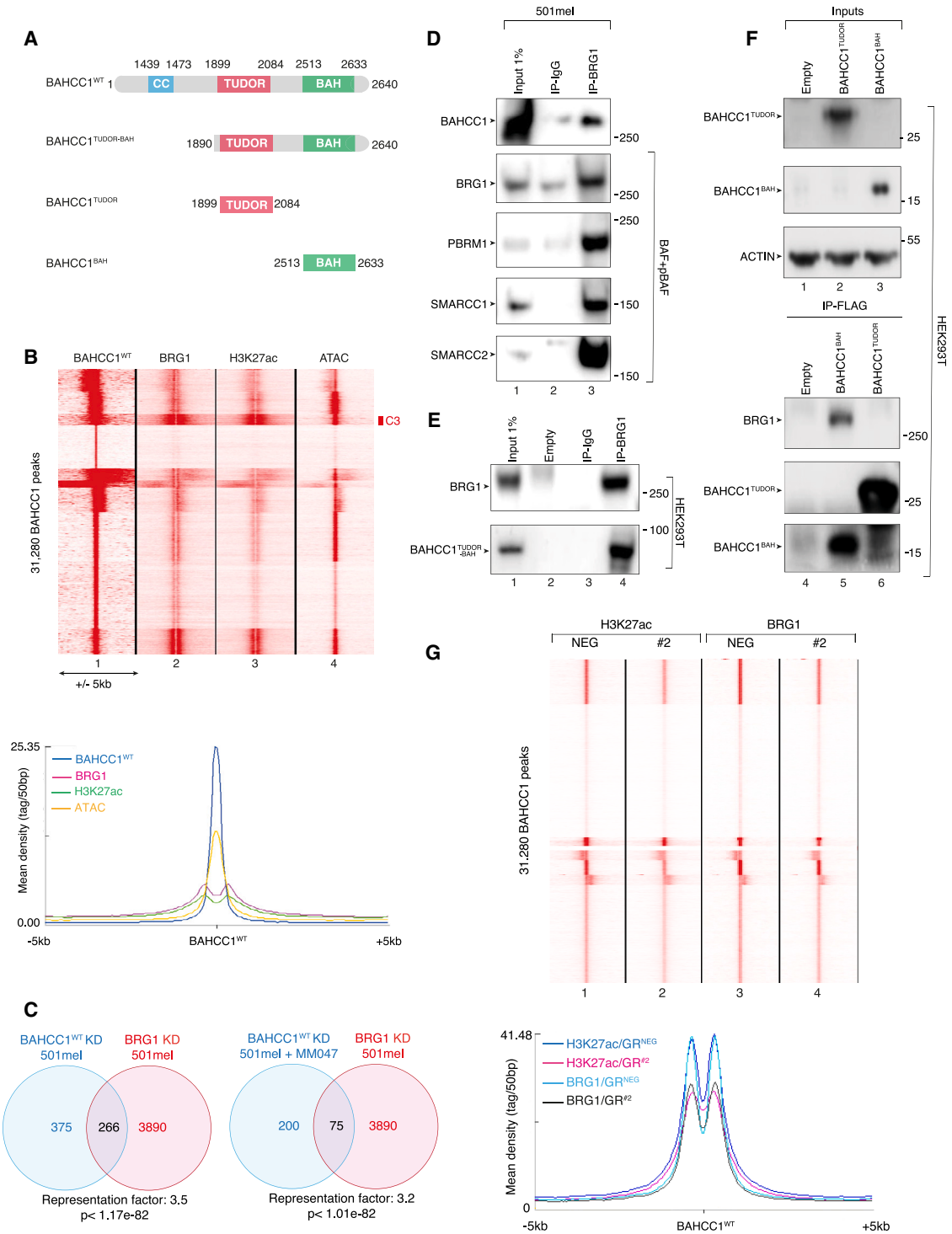

Figure 6. BAHCC1 interacts with BRG1-containing chromatin remodeler complexes

(A) Domain architecture of BAHCC1. CC, coiled coil. The deletion mutants used below are shown.

(B) Top: read density clustering using seqMINER showing the co-localization between BAHCC1^{WT}, BRG1, H3K27ac, and ATAC signals in the 31,280 BAHCC1-occupied sites. Cluster 3 (C3) is highlighted. Bottom: meta-profiles of BAHCC1, BRG1, H3K27ac and ATAC signals around the 31,280 BAHCC1 peaks.

(C) Left: Venn diagram showing the overlap between the downregulated genes in 501mel following either BRG1 or BAHCC1 KD. Right: Venn diagram showing the overlap between the downregulated genes in mel501 after BRG1 KD and the common downregulated genes in 501mel and MM047 after BAHCC1 KD. Representation factor and p values were calculated using hypergeometric test.

(legend continued on next page)

(Figure S5H), confirming its potential role in the control of the cell cycle in melanoma cells. Similar observations were made using TCGA datasets from patients with UVM or SKCM in which BAHCC1 expression significantly correlated with the Tirosh cell-cycle signature (Figure S5I). Together, these results demonstrate that BAHCC1 regulates the expression of a set of E2F/KLF-dependent genes involved in cell cycle and DNA repair.

BAHCC1 interacts with BRG1-containing complexes

Protein Blast and AlphaFold tools revealed the presence of a coiled-coil (CC) region in the central part of BAHCC1 together with two well-conserved TUDOR and BAH domains at the C terminus (Figure 6A). CCs are involved in protein-protein interactions, while BAH and TUDOR domains are found in a wide range of chromatin-binding proteins, where they are readers of histone modifications and act as chromatin co-activators/repressors.[34,35] We profiled genome occupancy of a FLAG-tagged truncated form of BAHCC1 missing the N-terminal CC domain and bearing only the short C-terminal region containing the TUDOR and BAH domains (BAHCC1$^{TUDOR-BAH}$) (Figure 6A). Genome-wide BAHCC1$^{TUDOR-BAH}$ occupancy pattern highly overlapped with endogenous BAHCC1^{WT}, as shown by seqMINER read density heatmap (Figure S6A), further validating the CUT&Tag data obtained above with the full-length endogenous protein. However, a limited cluster of sites was selectively occupied by endogenous BAHCC1^{WT} but not by the truncated form (Figure S6A; Table S6). This BAHCC1 N-terminal region-dependent cluster included 222 of the 539 genes downregulated after BAHCC1 KD, including DNA-repair or cell-cycle genes such as ATM or CDKN1A (Table S6). In agreement with this, RSAT analyses showed that N-terminal region-dependent sites were preferentially enriched in KLF-family DNA-binding motifs similar to the down-regulated promoters (Table S4).

We previously demonstrated that the BRG1 subunit of the PBAF chromatin remodeling complex occupied H3K27ac-marked nucleosomes in 501mel melanoma cells.[25] Comparison of genome-wide occupancy of both BRG1 and BAHCC1 showed that most BAHCC1 peaks were flanked by nucleosomes bound by BRG1 and marked by H3K27ac (Figure 6B). seqMINER read density clustering allowed the identification of several BAHCC1-BRG1 clusters, among which cluster 3 (C3) was associated with DNA-repair and cell-cycle genes including ATM, which was strongly enriched in BAHCC1, BRG1, and H3K27ac at its promoter (Figure S6B). Moreover, a significant fraction of genes downregulated upon BAHCC1 KD in 501mel were also downregulated by BRG1 silencing (Figure 6C, left), including 75 of the 200 genes downregulated in both 501mel and MM047 (Figure 6C, right). Most of these genes were found to be involved in mitosis and DNA repair, including ATM (Figures S6C and S6D; Table S3).

We next aimed to investigate whether a physical interaction could be observed between BAHCC1 and BRG1-containing complexes. BRG1 co-immunoprecipitated with endogenous BAHCC1, together with the BAF/pBAF subunits PBRM1, SMARCC1, and SMARCC2 in 501mel cells (Figure 6D). In parallel, pull-down of BRG1 co-precipitated the FLAG-tagged BAHCC1$^{TUDOR-BAH}$-deletion mutant overexpressed in HEK293T cells (Figure 6E). We further observed that BRG1 co-precipitated specifically with the BAH domain of BAHCC1 but not with the TUDOR domain (Figure 6F). The BAHCC1^{BAH}-BRG1 co-precipitation was confirmed in 501mel melanoma cells stably expressing the hemagglutinin (HA)-tagged BAHCC1^{BAH} domain (Figure S6E).

Moreover, both H3K27ac and BRG1 genomic occupancies were reduced around BAHCC1-binding sites following BAHCC1 KD (Figure 6G). Altogether, these data highlight a direct physical interaction between BAHCC1 and BRG1-containing BAF and PBAF complexes, which impacts BRG1 recruitment and H3K27ac deposition around BAHCC1-binding sites.

BAHCC1 KD cooperates with PARP inhibition to induce melanoma cell death

The above results suggested a role of BAHCC1 in genome stability through its regulation of DNA-repair proteins, including the master DNA damage repair sensor ATM. In agreement, qRT-PCR and immunoblotting showed that BAHCC1 KD decreased expression of ATM at the mRNA and protein levels (Figures 7A and 7B), which can be explained by a loss of H3K27ac deposition and BRG1 recruitment at its promoter (Figure S7A). Furthermore, BAHCC1 expression positively correlated with genome alteration frequencies in human melanoma tumors (Figure 7C). We then tested the effect of BAHCC1 KD on the ability of 501mel cells to repair DNA following treatment with neocarzinostatin (NCS), which induces DNA double-strand breaks (Figure 7D). Strikingly, BAHCC1 KD led to higher numbers of γH2AX foci during the repair time course, indicating a delay in the repair of DNA double-strand breaks in the absence of BAHCC1 (Figures 7E and S7B).

PARP1 is the main PARP-family protein involved in DNA damage response, where it acts as a DNA damage sensor. PARP1 inhibition (PARPi) has been shown to increase DNA replication fork destabilization, leading to accumulation of DNA breaks.[36] Since the PARP pathway acts independently from ATM, it has been postulated that ATM-deficient cancer cells become addicted to PARP-dependent DNA repair, making them highly sensitive to PARPi.[37] Therefore, we queried whether BAHCC1 KD might

(D) BRG1 was immunoprecipitated (IP-BRG1) from nuclear extracts of 501mel cells. Following SDS-PAGE, proteins were immunoblotted as indicated, including subunits of the pBAF/BAF complexes. IP-IgG was performed as a negative control. Molecular sizes are indicated.
(E) HEK293T cells were transfected to express HA-BAHCC1$^{TUDOR-BAH}$ protein and BRG1 was IP (IP-BRG1). Following SDS-PAGE, proteins were immunoblotted as indicated. IP-IgG was performed as a negative control. Molecular sizes are indicated.
(F) HEK293T cells were transfected to express FLAG-BAHCC1^{BAH} and FLAG-BAHCC1^{TUDOR} domains, and FLAG-IP was performed. Following SDS-PAGE, proteins were immunoblotted as indicated. Molecular sizes are indicated.
(G) Top: read density clustering using seqMINER showing the co-localization between H3K27ac and BRG1 signals in the 31,280 H3K27ac-deposition sites with (GR^{NEG}) or without BAHCC1 (GR$^{\#2}$). Bottom: meta-profiles of H3K27ac and BRG1 signals around the 31,280 H3K27ac peaks with (GR^{NEG}) or without (GR$^{\#2}$) BAHCC1.

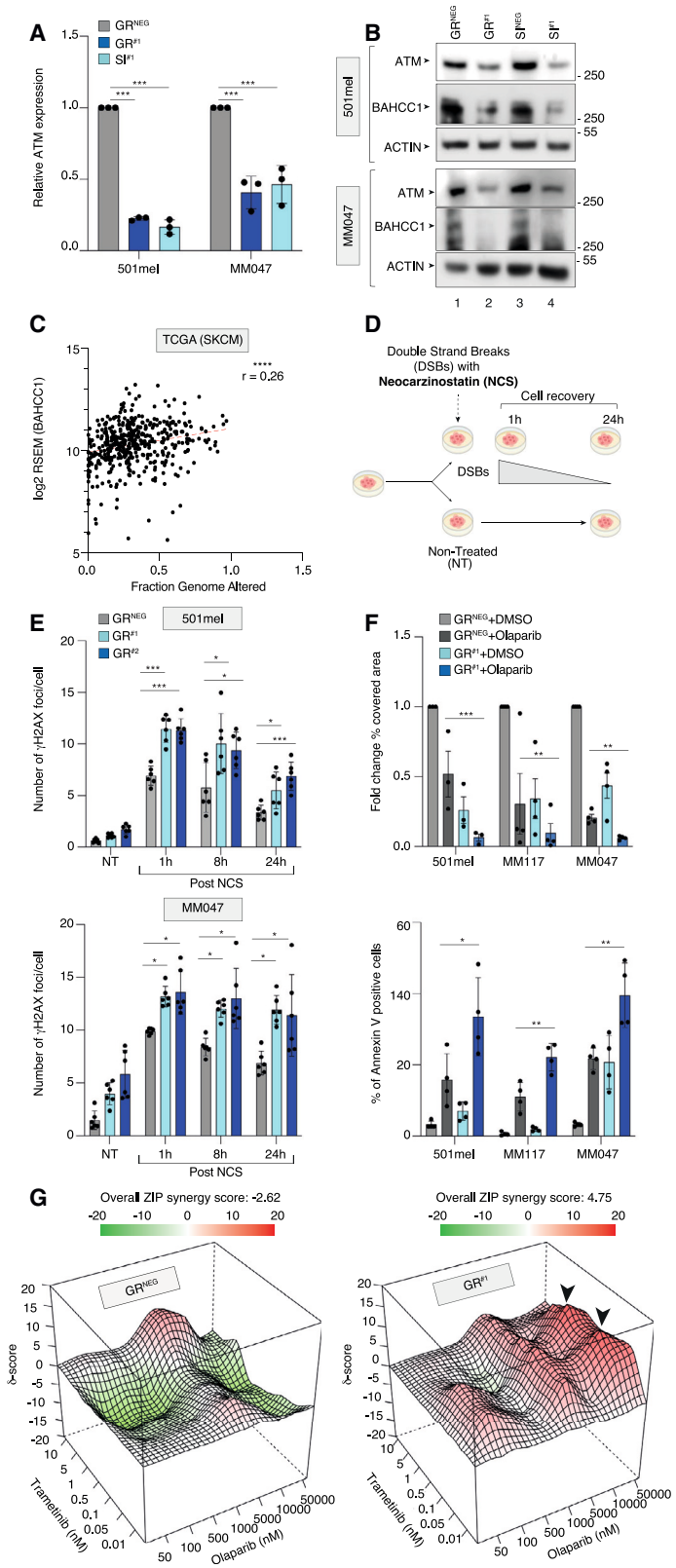

Figure 7. BAHCC1 depletion cooperates with PARPi to induce cell death

(A) Relative ATM expression upon transfection with GR^{NEG}, $GR^{\#1}$, and shBAHCC1 was measured by qRT-PCR in 501mel or MM047. Bars represent mean values of three different experiments (biological triplicates) (±SEM). Two-way ANOVA using Šídák's multiple comparisons test.

(B) 501mel or MM047 was transfected with GR^{NEG}, $GR^{\#1}$, siCTRL (SI^{NEG}), or shBAHCC1 ($SI^{\#1}$). Whole-cell extracts were resolved by SDS-PAGE, and proteins were immunoblotted as indicated.

(C) Spearman correlation between BAHCC1 expression and the fraction of genomic alteration (FGA) in TCGA melanoma samples (n = 443), where FGA is considered as the percentage of copy-number alterations found in the tumor compared to the healthy karyotype. The linear regression curve is shown in red.

(D) Schematic representation of the *in vitro* experiments using neocarzinostatin (NCS).

(E) Immunofluorescence quantification of the number of γH2AX foci per cell in 501mel and MM047 transfected either with GR^{NEG}, $GR^{\#1}$, or $GR^{\#2}$ and treated or not (NT) with NCS (1, 8, and 24 h recovery). Bars represent the means obtained from six biological replicates (±SEM) (501mel n1 = 45,338, n2 = 46,604, n3 = 47,365, n4 = 39,185, n5 = 61,975, n6 = 85,783; MM047 n1 = 26,535, n2 = 26,284, n3 = 28,105, n4 = 8,559, n5 = 13,342, n6 = 18,296). Two-way ANOVA test.

(F) Left: crystal violet quantification expressed as fold change relative to GR^{NEG}-transfected cells treated with DMSO. Bars represent mean values of three different experiments (biological triplicates) (±SEM). Two-way ANOVA using Dunnett's multiple comparisons test. Right: percentage of annexin V-positive cells in 501mel, MM117, and MM047 transfected with GR^{NEG} and $GR^{\#1}$ and treated for 96 h with DMSO or 10 μM olaparib. Bars represent mean values of three different experiments (biological triplicates) (±SEM). Two-way ANOVA using Dunnett's multiple comparisons test.

(G) Surface plot in three-dimensional views, showing synergy scores for impact of trametinib plus olaparib combination on 501mel cell viability. Cells were transfected with GR^{NEG} and $GR^{\#1}$. ZIP synergy scores (shown as d-scores) were calculated from the percentage of inhibition of 501mel cell viability in the dose combination matrix. Black arrows indicate the areas of the most synergistic scores (ZIP > 10). Areas in red, white, and green show regions of synergy, additivity, and antagonism, respectively.

potentiate the effect of PARPi in melanoma cells. Strikingly, co-treatment with the PARPi olaparib and BAHCC1 KD showed a significant cooperative effect on viability of 501mel (MITF^{HIGH}, BRAF^{V600E}), MM117 (MITF^{HIGH}, triple WT), and MM047 (MITF^{LOW}, NRAS^{Q61R}) melanoma cells due to increased apoptosis (Figure 7F). We additionally tested the impact of the combination of PARPi and targeted therapies on the viability of 501mel cells with or without BAHCC1 with SynergyFinder, using the Zero Interaction Potency (ZIP) model. In the absence of BAHCC1, the overall positive ZIP score of 4.45 suggested moderate synergy between the two drugs, which was highest at intermediate and high concentrations of olaparib (ZIP $\geq$ 10), regardless of the concentration of trametinib (Figure 7G, right). The negative ZIP score in the presence of BAHCC1 (Figure 7G, left) suggested that it was the absence of BAHCC1 that induced the moderate synergism observed above. Overall, these findings demonstrate the important role of BAHCC1 in the expression of DNA-repair genes such as ATM, and the kinetics of DNA repair are in line with the idea that melanoma cells may be sensitized to PARPi by BAHCC1 depletion.

DISCUSSION

Deregulation of gene expression in cancer cells is well established and cannot always be explained solely by genomic alterations such as mutations or copy-number variations. Cancer cells undergo significant changes in their transcriptional program through extensive rewiring that includes the acquisition of alternative gene regulatory elements such as SEs.[1,23,38] Using several H3K27ac ChIP-seq datasets from short-term patient-derived cutaneous melanoma cultures, we identified melanoma-specific SEs and their associated genes as potential targets for therapy. We further integrated the H3K27ac profile with the binding profiles of master regulators in melanoma cells such as SOX10 and MITF, which occupy long and short enhancers found in cutaneous melanocytic-like melanoma cells, with SOX10 being required to achieve high levels of activity.[27] Our analysis converged on the SE17q25 element that was activated in most melanocytic-like melanoma cells, regardless of driver mutation status. In cutaneous melanoma cells, the SE17q25 element was not only highly occupied by MITF and SOX10 but also by the TFIIH kinase CDK7 and BRG1, all of which are known to occupy relevant SEs.[5,39,40] Depletion of MITF or SOX10 as well as TFIIH inhibition decommissioned SE17q25 and reduced the expression of BAHCC1, a gene located in close vicinity to SE17q25. In addition, selective CRISPR-mediated silencing of SE17q25 significantly affected BAHCC1 expression, strongly supporting the idea that SE17q25 regulated BAHCC1 expression. These observations in cultured cells were validated using TCGA data on human tumors showing that SE17q25 activity positively correlates with BAHCC1 expression. Importantly, SE17q25 activity and BAHCC1 expression are highest in SKCM compared to other tumors.

In agreement with its dependency on MITF and SOX10 observed *in vitro*, high BAHCC1 expression correlated with high MITF and SOX10 expression in melanoma biopsies and with poor prognosis in both patients with SKCM and with UVM.[41] Consistent with these findings, an extensive analysis of single-cell transcriptomic data from melanoma PDXs demonstrated that BAHCC1 expression was the highest in "mitotic-like" cells.[26] "Mitotic-like" melanoma cells have been found in metastatic SKCM and UVM biopsies and are characterized by expression of E2F-dependent genes. E2F transcription factors are known to promote melanoma progression and metastasis.[42,43] These data are consistent with the fact that our *in vitro* and *in vivo* functional studies showed that BAHCC1 was essential for melanoma cell proliferation and tumor growth by regulating a set of E2F/KLF-dependent genes. Although MITF^{LOW} cells have significantly reduced SE17q25 activity and BAHCC1 expression, we observed that they also depend on SE17q25 and BAHCC1, whose expression may be differently regulated by other TFs important for the mesenchymal state such as TFAP2A, FOSL2, and TEAD4 that bind within SE17q25.[8,16,19,27]

BAH domains are known to bind post-translation modifications (PTMs) of histones such as H3K27me3[44,45] and H4K20me2.[46,47] A previous study characterized the BAHCC1 BAH domain, showing that it binds H3K27me3 and that BAHCC1 interacts with histone deacetylases (HDACs) and SAP30BP proteins of the polycomb repressor complex 1 (PRC1) in acute myeloid leukemia (AML) to repress a large number of genes involved in myeloid differentiation and to promote cell proliferation.[45] In melanoma, BAHCC1 did not show a predominant repressive role, as an equivalent number of genes were up- and downregulated after BAHCC1 KD. CUT&Tag performed on H3K27me3 in 501mel demonstrated that this mark was not present around the BAHCC1-binding sites (Figures S8A and S8B). These observations support the idea that BAHCC1 activity in melanoma does not depend on BAH-H3K27me3 interactions. Our data demonstrated an interaction between BAHCC1 and the SWI/SNF chromatin remodeling complexes, occurring through the BAHCC1^{BAH} domain. We postulate that BRG1 may act upstream to remodel the chromatin, creating the nucleosome-depleted regions to be occupied by BAHCC1. Alternatively, BAHCC1 may be recruited to chromatin via interaction with transcription factors such as those of the KLF/SP/E2F families to regulate their target genes. Moreover, the N-terminal region of BAHCC1, containing the CC domain, appears to be important for the recruitment of BAHCC1 to a set of genes involved in cell proliferation and DNA repair, again suggesting that the BAH domain is not the only determinant of genomic recruitment. We therefore propose that either or both of the above mechanisms drive BAHCC1 genomic recruitment in melanoma, in stark contrast to the BAH-H3K27me3 pathway in AML.

Metastatic melanoma is characterized by the overexpression of genes involved in the DNA damage response (DDR), which makes this tumor stage highly refractory to chemo- and radiotherapies.[48] DDR is essential for maintaining genomic stability to face genotoxic stress resulting from environmental and endogenous DNA damage. In the DDR, ATM, the pivotal mediator of genotoxic stress, phosphorylates histone H2AX to γH2AX to generate docking sites for proteins involved in DNA break repair. ATM also links DNA damage to the cell cycle by controlling key DNA damage checkpoints to regulate DNA break repair directly or indirectly though the control of cell-cycle

checkpoints. On the other hand, PARP1 is able to bind to damaged DNA sites to promote the PARylation of surrounding proteins, thus creating new scaffolds for the recruitment of DNA-repair proteins involved in an alternative DNA break repair pathway. This dual DNA-repair mechanism ensures that DNA breaks are repaired efficiently. However, the loss of one DNA-repair pathway results in increased reliance on the other, which is not essential under healthy settings. Therefore, a high response rate to the PARP inhibitor olaparib was found in patients with metastatic prostate[49] or gastric[50] cancers harboring low expression or mutations of ATM. Since ATM was one of the E2F-dependent genes strongly regulated by BAHCC1, we wondered if this dependence could be exploited therapeutically. Interestingly, BAHCC1 KD cooperates with PARP inhibition by olaparib to impact cell survival, associated with increased apoptosis. In addition to their potential clinical application, these data clearly demonstrate the involvement of BAHCC1 in the control of genes involved in DDR in melanoma cells and suggest that metastatic melanoma upregulates BAHCC1 to promote genomic stability and cellular fitness necessary to sustain high mitotic rates. Finally, the presence of a gene expressed in both cutaneous melanoma and UVM cells makes it possible to envisage common treatments for these two cancers.

Limitations of the study

Our study shows the involvement of BAHCC1 in melanoma growth and maintenance. We show that BAHCC1 is a transcription factor involved in regulating the expression of genes involved in cell-cycle progression and DNA repair. Although we have shown the link between BAHCC1 and BRG1-containing transcription complexes, we have not demonstrated the precise molecular role of BAHCC1 in melanoma. We assume that it interacts with BAF/pBAF complexes to facilitate their recruitment to the promoters of these genes, but we have not demonstrated this hypothesis.

STAR★METHODS

Detailed methods are provided in the online version of this paper and include the following:

SUPPLEMENTAL INFORMATION

Supplemental information can be found online at https://doi.org/10.1016/j.celrep.2023.113363.

ACKNOWLEDGMENTS

We thank the IGBMC facilities, in particular Paola Rossolillo and Karim Essabri for the isolation of BAHCC1 cDNA, and Dr. Catherine Birck and Dr. Nathalie Troffer-Charlier for the purification of the BAH and TUDOR domains. We thank Prof D. Lipsker and the staff of the Strasbourg University Hospital dermatology clinic for tumor sections and Prof. G. Ghanem and Prof. J.-C. Marine for providing us with the MM-series melanoma cultures. This study was supported by the Institut National Du Cancer (INCa) (INCa_18353, F.C. and I.D.); the Ligue Contre le Cancer (Equipe labélisée 2022, F.C. and I.D.); the Fondation ARC; and the ANR-10-LABX-0030-INRT, a French State fund managed by the Agence Nationale de la Recherche under the frame program Investissements d'Avenir ANR-10- IDEX-0002-02. Sequencing was performed by the IGBMC GenomEast platform, a member of the "France Génomique" consortium (ANR-10-INBS-0009). E.H. is funded by R01CA243446, R01CA274100, U54 CA263001, and R01CA277425 (NCI/NIH). P.B. has been supported by the Ligue contre le Cancer and the National Cancer Center. We thank the NYULH Preclinical imaging (Orlando Aristizabal), Experimental Pathology (Cindy Loomis, Mark Alu), and Microscopy Core facilities, all partially supported by the Cancer Center Support Grant (CCSG) from NCI/NIH to the Perlmutter Cancer Center P30CA016087 (PI: B. Nsel).

AUTHOR CONTRIBUTIONS

P.B., I.D., and F.C. conceived the study. P.B., I.D., and F.C. analyzed the data. P.B. performed most of the *in vitro* functional studies, RNA-seq, and RNAScope. P.B. and M.N. performed qRT-PCR and WB. S.L.G., G.D., T.Y., and P.B., performed bioinformatic analyses. B.H.V., A.L., and M.C. performed wet lab of CUT&Tag experiments. M.C. performed the Boyden chamber experiments. J.O. performed the SynergyFinder experiment. P.B., M.N., and L.S. performed immunoprecipitation. E.H. supervised the *in vivo* studies and provided feedback on the manuscript. P.B., F.V.-R., A.F.-Y., and C.F.C. performed *in vivo* experiments. G.M., G.G., M.D., E.C., and C.B. provided valuable materials. F.C., I.D., and P.B wrote the manuscript.

DECLARATION OF INTERESTS

The authors declare no competing interests.

Received: November 2, 2022
Revised: July 27, 2023
Accepted: October 16, 2023
Published: November 3, 2023

REFERENCES

1. Bradner, J.E., Hnisz, D., and Young, R.A. (2017). Transcriptional Addiction in Cancer. Cell *168*, 629–643. https://doi.org/10.1016/j.cell.2016.12.013.

2. Hnisz, D., Abraham, B.J., Lee, T.I., Lau, A., Saint-André, V., Sigova, A.A., Hoke, H.A., and Young, R.A. (2013). Super-enhancers in the control of cell identity and disease. Cell *155*, 934–947. https://doi.org/10.1016/j.cell.2013.09.053.

3. Pott, S., and Lieb, J.D. (2015). What are super-enhancers? Nat. Genet. *47*, 8–12. https://doi.org/10.1038/ng.3167.

4. Filippakopoulos, P., Qi, J., Picaud, S., Shen, Y., Smith, W.B., Fedorov, O., Morse, E.M., Keates, T., Hickman, T.T., Felletar, I., et al. (2010). Selective inhibition of BET bromodomains. Nature *468*, 1067–1073. https://doi.org/10.1038/nature09504.

5. Kwiatkowski, N., Zhang, T., Rahl, P.B., Abraham, B.J., Reddy, J., Ficarro, S.B., Dastur, A., Amzallag, A., Ramaswamy, S., Tesar, B., et al. (2014). Targeting transcription regulation in cancer with a covalent CDK7 inhibitor. Nature *511*, 616–620. https://doi.org/10.1038/nature13393.

6. Postel-Vinay, S., Herbschleb, K., Massard, C., Woodcock, V., Soria, J.-C., Walter, A.O., Ewerton, F., Poelman, M., Benson, N., Ocker, M., et al. (2019). First-in-human phase I study of the bromodomain and extraterminal motif inhibitor BAY 1238097: emerging pharmacokinetic/pharmacodynamic relationship and early termination due to unexpected toxicity. Eur. J. Cancer *109*, 103–110.

7. Ameratunga, M., Braña, I., Bono, P., Postel-Vinay, S., Plummer, R., Aspegren, J., Korjamo, T., Snapir, A., and de Bono, J.S. (2020). First-in-human Phase 1 open label study of the BET inhibitor ODM-207 in patients with selected solid tumours. Br. J. Cancer *123*, 1730–1736. https://doi.org/10.1038/s41416-020-01077-z.

8. Fontanals-Cirera, B., Hasson, D., Vardabasso, C., Di Micco, R., Agrawal, P., Chowdhury, A., Gantz, M., de Pablos-Aragoneses, A., Morgenstern, A., Wu, P., et al. (2017). Harnessing BET Inhibitor Sensitivity Reveals AMIGO2 as a Melanoma Survival Gene. Mol. Cell *68*, 731–744.e9. https://doi.org/10.1016/j.molcel.2017.11.004.

9. Ribas, A., Read, P., and Slingluff, C. (2015). Cutaneous Melanoma. In Rosenberg's Cancer: Principles and Practice of Oncology, H. DeVita, ed. (Wolters Kluwer).

10. Mitchell, T., Karakousis, G., and Schuchter, L. (2020). Melanoma. In Abeloff's Clinical Oncology Abeloff's Clinical Oncology, J.E. Niederhuber, J.O. Armitage, J.H. Doroshow, M.B. Kastan, and J.E. Tepper, eds. (Elsevier).

11. Chapman, P.B., Hauschild, A., Robert, C., Haanen, J.B., Ascierto, P., Larkin, J., Dummer, R., Garbe, C., Testori, A., Maio, M., et al. (2011). Improved Survival with Vemurafenib in Melanoma with BRAF V600E Mutation. N. Engl. J. Med. *364*, 2507–2516. https://doi.org/10.1056/NEJMoa1103782.

12. Robert, C., Grob, J.J., Stroyakovskiy, D., Karaszewska, B., Hauschild, A., Levchenko, E., Chiarion Sileni, V., Schachter, J., Garbe, C., Bondarenko, I., et al. (2019). Five-Year Outcomes with Dabrafenib plus Trametinib in Metastatic Melanoma. N. Engl. J. Med. *381*, 626–636. https://doi.org/10.1056/NEJMoa1904059.

13. Curti, B.D., and Faries, M.B. (2021). Recent Advances in the Treatment of Melanoma. N. Engl. J. Med. *384*, 2229–2240. https://doi.org/10.1056/NEJMra2034861.

14. Marin-Bejar, O., Rogiers, A., Dewaele, M., Femel, J., Karras, P., Pozniak, J., Bervoets, G., Van Raemdonck, N., Pedri, D., Swings, T., et al. (2021). Evolutionary predictability of genetic versus nongenetic resistance to anticancer drugs in melanoma. Cancer Cell *39*, 1135–1149.e8. https://doi.org/10.1016/j.ccell.2021.05.015.

15. Rubanov, A., Berico, P., and Hernando, E. (2022). Epigenetic Mechanisms Underlying Melanoma Resistance to Immune and Targeted Therapies. Cancers *14*, 5858. https://doi.org/10.3390/cancers14235858.

16. Verfaillie, A., Imrichova, H., Atak, Z.K., Dewaele, M., Rambow, F., Hulselmans, G., Christiaens, V., Svetlichnyy, D., Luciani, F., Van Den Mooter, L., et al. (2015). Decoding the regulatory landscape of melanoma reveals TEADS as regulators of the invasive cell state. Nat. Commun. *6*, 6683. https://doi.org/10.1038/ncomms7683.

17. Rambow, F., Rogiers, A., Marin-Bejar, O., Aibar, S., Femel, J., Dewaele, M., Karras, P., Brown, D., Chang, Y.H., Debiec-Rychter, M., et al. (2018). Toward Minimal Residual Disease-Directed Therapy in Melanoma. Cell *174*, 843–855.e19. https://doi.org/10.1016/j.cell.2018.06.025.

18. Rambow, F., Marine, J.C., and Goding, C.R. (2019). Melanoma plasticity and phenotypic diversity: Therapeutic barriers and opportunities. Genes Dev. *33*, 1295–1318. https://doi.org/10.1101/gad.329771.119.

19. Wouters, J., Kalender-Atak, Z., Minnoye, L., Spanier, K.I., De Waegeneer, M., Bravo González-Blas, C., Mauduit, D., Davie, K., Hulselmans, G., Najem, A., et al. (2020). Robust gene expression programs underlie recurrent cell states and phenotype switching in melanoma. Nat. Cell Biol. *22*, 986–998. https://doi.org/10.1038/s41556-020-0547-3.

20. Onken, M.D., Worley, L.A., Long, M.D., Duan, S., Council, M.L., Bowcock, A.M., and Harbour, J.W. (2008). Oncogenic Mutations in *GNAQ* Occur Early in Uveal Melanoma. Invest. Ophthalmol. Vis. Sci. *49*, 5230–5234. https://doi.org/10.1167/iovs.08-2145.

21. Van Raamsdonk, C.D., Griewank, K.G., Crosby, M.B., Garrido, M.C., Vemula, S., Wiesner, T., Obenauf, A.C., Wackernagel, W., Green, G., Bouvier, N., et al. (2010). Mutations in *GNA11* in Uveal Melanoma. N. Engl. J. Med. *363*, 2191–2199. https://doi.org/10.1056/NEJMoa1000584.

22. Yang, J., Manson, D.K., Marr, B.P., and Carvajal, R.D. (2018). Treatment of uveal melanoma: where are we now? Ther. Adv. Med. Oncol. *10*, 1758834018757175. https://doi.org/10.1177/1758834018757175.

23. Lovén, J., Hoke, H.A., Lin, C.Y., Lau, A., Orlando, D.A., Vakoc, C.R., Bradner, J.E., Lee, T.I., and Young, R.A. (2013). Selective inhibition of tumor oncogenes by disruption of super-enhancers. Cell *153*, 320–334. https://doi.org/10.1016/j.cell.2013.03.036.

24. Strub, T., Giuliano, S., Ye, T., Bonet, C., Keime, C., Kobi, D., Le Gras, S., Cormont, M., Ballotti, R., Bertolotto, C., and Davidson, I. (2011). Essential role of microphthalmia transcription factor for DNA replication, mitosis and genomic stability in melanoma. Oncogene *30*, 2319–2332. https://doi.org/10.1038/onc.2010.612.

25. Laurette, P., Strub, T., Koludrovic, D., Keime, C., Le Gras, S., Seberg, H., Van Otterloo, E., Imrichova, H., Siddaway, R., Aerts, S., et al. (2015). Transcription factor MITF and remodeller BRG1 define chromatin organisation at regulatory elements in melanoma cells. Elife *4*, e06857. https://doi.org/10.7554/eLife.06857.

26. Berico, P., Cigrang, M., Davidson, G., Braun, C., Sandoz, J., Legras, S., Vokshi, B.H., Slovic, N., Peyresaubes, F., Gene Robles, C.M., et al. (2021). CDK7 and MITF repress a transcription program involved in survival and drug tolerance in melanoma. EMBO Rep. *22*, e51683. https://doi.org/10.15252/embr.202051683.

27. Mauduit, D., Taskiran, I.I., Minnoye, L., de Waegeneer, M., Christiaens, V., Hulselmans, G., Demeulemeester, J., Wouters, J., and Aerts, S. (2021). Analysis of long and short enhancers in melanoma cell states. Elife *10*, e71735. https://doi.org/10.7554/eLife.71735.

28. Chipumuro, E., Marco, E., Christensen, C.L., Kwiatkowski, N., Zhang, T., Hatheway, C.M., Abraham, B.J., Sharma, B., Yeung, C., Altabef, A., et al. (2014). CDK7 inhibition suppresses super-enhancer-linked oncogenic transcription in MYCN-driven cancer. Cell *159*, 1126–1139. https://doi.org/10.1016/j.cell.2014.10.024.

29. Titov, D.V., Gilman, B., He, Q.L., Bhat, S., Low, W.K., Dang, Y., Smeaton, M., Demain, A.L., Miller, P.S., Kugel, J.F., et al. (2011). XPB, a subunit of TFIIH, is a target of the natural product triptolide. Nat. Chem. Biol. *7*, 182–188. https://doi.org/10.1038/nchembio.522.

30. Noel, P., Hussein, S., Ng, S., Antal, C.E., Lin, W., Rodela, E., Delgado, P., Naveed, S., Downes, M., Lin, Y., et al. (2020). Triptolide targets super-enhancer networks in pancreatic cancer cells and cancer-associated fibroblasts. Oncogenesis *9*, 100. https://doi.org/10.1038/s41389-020-00285-9.

31. Sun, Q., Lee, W., Mohri, Y., Takeo, M., Lim, C.H., Xu, X., Myung, P., Atit, R.P., Taketo, M.M., Moubarak, R.S., et al. (2019). A novel mouse model demonstrates that oncogenic melanocyte stem cells engender melanoma

resembling human disease. Nat. Commun. *10*, 5023. https://doi.org/10.1038/s41467-019-12733-1.

32. Tirosh, I., Izar, B., Prakadan, S.M., Wadsworth, M.H., Treacy, D., Trombetta, J.J., Rotem, A., Rodman, C., Lian, C., Murphy, G., et al. (2016). Dissecting the multicellular ecosystem of metastatic melanoma by single-cell RNA-seq. Science *352*, 189–196. https://doi.org/10.1126/science.aad0501.
33. Pandiani, C., Strub, T., Nottet, N., Cheli, Y., Gambi, G., Bille, K., Husser, C., Dalmasso, M., Béranger, G., Lassalle, S., et al. (2021). Single-cell RNA sequencing reveals intratumoral heterogeneity in primary uveal melanomas and identifies HES6 as a driver of the metastatic disease. Cell Death Differ. *28*, 1990–2000. https://doi.org/10.1038/s41418-020-00730-7.
34. Ciani, B., Bjelić, S., Honnappa, S., Jawhari, H., Jaussi, R., Payapilly, A., Jowitt, T., Steinmetz, M.O., and Kammerer, R.A. (2010). Molecular basis of coiled-coil oligomerization-state specificity. Proc. Natl. Acad. Sci. USA *107*, 19850–19855. https://doi.org/10.1073/pnas.1008502107.
35. Musselman, C.A., Lalonde, M.-E., Côté, J., and Kutateladze, T.G. (2012). Perceiving the epigenetic landscape through histone readers. Nat. Struct. Mol. Biol. *19*, 1218–1227. https://doi.org/10.1038/nsmb.2436.
36. Caron, M.C., Sharma, A.K., O'Sullivan, J., Myler, L.R., Ferreira, M.T., Rodrigue, A., Coulombe, Y., Ethier, C., Gagné, J.P., Langelier, M.F., et al. (2019). Poly(ADP-ribose) polymerase-1 antagonizes DNA resection at double-strand breaks. Nat. Commun. *10*, 2954. https://doi.org/10.1038/s41467-019-10741-9.
37. Pilié, P.G., Gay, C.M., Byers, L.A., O'Connor, M.J., and Yap, T.A. (2019). PARP Inhibitors: Extending Benefit Beyond *BRCA* -Mutant Cancers. Clin. Cancer Res. *25*, 3759–3771. https://doi.org/10.1158/1078-0432.CCR-18-0968.
38. Lee, T.I., and Young, R.A. (2013). Transcriptional regulation and its misregulation in disease. Cell *152*, 1237–1251. https://doi.org/10.1016/j.cell.2013.02.014.
39. Barutcu, A.R., Lajoie, B.R., Fritz, A.J., McCord, R.P., Nickerson, J.A., Van Wijnen, A.J., Lian, J.B., Stein, J.L., Dekker, J., Stein, G.S., and Imbalzano, A.N. (2016). SMARCA4 regulates gene expression and higherorder chromatin structure in proliferating mammary epithelial cells. Genome Res. *26*, 1188–1201. https://doi.org/10.1101/gr.201624.115.
40. Eliades, P., Abraham, B.J., Ji, Z., Miller, D.M., Christensen, C.L., Kwiatkowski, N., Kumar, R., Njauw, C.N., Taylor, M., Miao, B., et al. (2018). High MITF Expression Is Associated with Super-Enhancers and Suppressed by CDK7 Inhibition in Melanoma. J. Invest. Dermatol. *138*, 1582–1590. https://doi.org/10.1016/j.jid.2017.09.056.
41. Gao, Y., Li, Y., Niu, X., Wu, Y., Guan, X., Hong, Y., Chen, H., and Song, B. (2020). Identification and Validation of Prognostically Relevant Gene Signature in Melanoma. BioMed Res. Int. *2020*, 5323614. https://doi.org/10.1155/2020/5323614.
42. Ma, Y., Kurtyka, C.A., Boyapalle, S., Sung, S.-S., Lawrence, H., Guida, W., and Cress, W.D. (2008). A Small-Molecule E2F Inhibitor Blocks Growth in a Melanoma Culture Model. Cancer Res. *68*, 6292–6299. https://doi.org/10.1158/0008-5472.CAN-08-0121.
43. Alla, V., Engelmann, D., Niemetz, A., Pahnke, J., Schmidt, A., Kunz, M., Emmrich, S., Steder, M., Koczan, D., and Pützer, B.M. (2010). E2F1 in Melanoma Progression and Metastasis. J. Natl. Cancer Inst. *102*, 127–133. https://doi.org/10.1093/jnci/djp458.
44. Zhao, D., Zhang, X., Guan, H., Xiong, X., Shi, X., Deng, H., and Li, H. (2016). The BAH domain of BAHD1 is a histone H3K27me3 reader. Protein Cell *7*, 222–226. https://doi.org/10.1007/s13238-016-0243-z.
45. Fan, H., Lu, J., Guo, Y., Li, D., Zhang, Z.M., Tsai, Y.H., Pi, W.C., Ahn, J.H., Gong, W., Xiang, Y., et al. (2020). BAHCC1 binds H3K27me3 via a conserved BAH module to mediate gene silencing and oncogenesis. Nat. Genet. *52*, 1384–1396. https://doi.org/10.1038/s41588-020-00729-3.
46. Kuo, A.J., Song, J., Cheung, P., Ishibe-Murakami, S., Yamazoe, S., Chen, J.K., Patel, D.J., and Gozani, O. (2012). ORC1 BAH domain links H4K20 to DNA replication licensing and Meier-Gorlin syndome. Nature *484*, 115–119. https://doi.org/10.1038/nature10956.ORC1.
47. Dai, Y., Zhang, A., Shan, S., Gong, Z., and Zhou, Z. (2018). Structural basis for recognition of 53BP1 tandem Tudor domain by TIRR. Nat. Commun. *9*, 2123. https://doi.org/10.1038/s41467-018-04557-2.
48. Kauffmann, A., Rosselli, F., Lazar, V., Winnepenninckx, V., Mansuet-Lupo, A., Dessen, P., Van Den Oord, J.J., Spatz, A., and Sarasin, A. (2008). High expression of DNA repair pathways is associated with metastasis in melanoma patients. Oncogene *27*, 565–573. https://doi.org/10.1038/sj.onc.1210700.
49. Mateo, J., Carreira, S., Sandhu, S., Miranda, S., Mossop, H., Perez-Lopez, R., Nava Rodrigues, D., Robinson, D., Omlin, A., Tunariu, N., et al. (2015). DNA-Repair Defects and Olaparib in Metastatic Prostate Cancer. N. Engl. J. Med. *373*, 1697–1708. https://doi.org/10.1056/NEJMoa1506859.
50. Bang, Y.-J., Im, S.-A., Lee, K.-W., Cho, J.Y., Song, E.-K., Lee, K.H., Kim, Y.H., Park, J.O., Chun, H.G., Zang, D.Y., et al. (2015). Randomized, Double-Blind Phase II Trial With Prospective Classification by ATM Protein Level to Evaluate the Efficacy and Tolerability of Olaparib Plus Paclitaxel in Patients With Recurrent or Metastatic Gastric Cancer. J. Clin. Orthod. *33*, 3858–3865. https://doi.org/10.1200/JCO.2014.60.0320.
51. Badal, B., Solovyov, A., Di Cecilia, S., Chan, J.M., Chang, L.W., Iqbal, R., Aydin, I.T., Rajan, G.S., Chen, C., Abbate, F., et al. (2017). Transcriptional dissection of melanoma identifies a high-risk subtype underlying TP53 family genes and epigenome deregulation. JCI Insight *2*, e92102. https://doi.org/10.1172/jci.insight.92102.
52. Yan, B.Y., Garcet, S., Gulati, N., Kiecker, F., Fuentes-Duculan, J., Gilleaudeau, P., Sullivan-Whalen, M., Shemer, A., Mitsui, H., and Krueger, J.G. (2019). Novel immune signatures associated with dysplastic naevi and primary cutaneous melanoma in human skin. Exp. Dermatol. *28*, 35–44. https://doi.org/10.1111/exd.13805.
53. Kabbarah, O., Nogueira, C., Feng, B., Nazarian, R.M., Bosenberg, M., Wu, M., Scott, K.L., Kwong, L.N., Xiao, Y., Cordon-Cardo, C., et al. (2010). Integrative Genome Comparison of Primary and Metastatic Melanomas. PLoS One *5*, e10770. https://doi.org/10.1371/journal.pone.0010770.
54. Xu, L., Shen, S.S., Hoshida, Y., Subramanian, A., Ross, K., Brunet, J.P., Wagner, S.N., Ramaswamy, S., Mesirov, J.P., and Hynes, R.O. (2008). Gene expression changes in an animal melanoma model correlate with aggressiveness of human melanoma metastases. Mol. Cancer Res. *6*, 760–769. https://doi.org/10.1158/1541-7786.MCR-07-0344.
55. Scatolini, M., Grand, M.M., Grosso, E., Venesio, T., Pisacane, A., Balsamo, A., Sirovich, R., Risio, M., and Chiorino, G. (2010). Altered molecular pathways in melanocytic lesions: Altered Molecular Pathways in Melanocytic Lesions. Int. J. Cancer *126*, 1869–1881. https://doi.org/10.1002/ijc.24899.
56. Ross-Innes, C.S., Stark, R., Teschendorff, A.E., Holmes, K.A., Ali, H.R., Dunning, M.J., Brown, G.D., Gojis, O., Ellis, I.O., Green, A.R., et al. (2012). Differential oestrogen receptor binding is associated with clinical outcome in breast cancer. Nature *481*, 389–393. https://doi.org/10.1038/nature10730.
57. Ramírez, F., Ryan, D.P., Grüning, B., Bhardwaj, V., Kilpert, F., Richter, A.S., Heyne, S., Dündar, F., and Manke, T. (2016). deepTools2: a next generation web server for deep-sequencing data analysis. Nucleic Acids Res. *44*, W160–W165. https://doi.org/10.1093/nar/gkw257.
58. Ye, T., Krebs, A.R., Choukrallah, M.-A., Keime, C., Plewniak, F., Davidson, I., and Tora, L. (2011). seqMINER: an integrated ChIP-seq data interpretation platform. Nucleic Acids Res. *39*, e35. https://doi.org/10.1093/nar/gkq1287.
59. Bailey, T.L., and Grant, C.E. (2021). SEA: Simple Enrichment Analysis of motifs. Preprint at bioRxiv. https://doi.org/10.1101/2021.08.23.457422.
60. Dobin, A., Davis, C.A., Schlesinger, F., Drenkow, J., Zaleski, C., Jha, S., Batut, P., Chaisson, M., and Gingeras, T.R. (2013). STAR: ultrafast universal RNA-seq aligner. Bioinformatics *29*, 15–21. https://doi.org/10.1093/bioinformatics/bts635.

61. Anders, S., and Huber, W. (2010). Differential expression analysis for sequence count data. Genome Biol. *11*, R106–R112. https://doi.org/10.1186/GB-2010-11-10-R106/COMMENTS.

62. Langmead, B., Trapnell, C., Pop, M., and Salzberg, S.L. (2009). Ultrafast and memory-efficient alignment of short DNA sequences to the human genome. Genome Biol. *10*, R25. https://doi.org/10.1186/gb-2009-10-3-r25.

63. Ennen, M., Keime, C., Gambi, G., Kieny, A., Coassolo, S., Thibault-Carpentier, C., Margerin-Schaller, F., Davidson, G., Vagne, C., Lipsker, D., and Davidson, I. (2017). MITF-High and MITF-Low Cells and a Novel Subpopulation Expressing Genes of Both Cell States Contribute to Intra- and Intertumoral Heterogeneity of Primary Melanoma. Clin. Cancer Res. *23*, 7097–7107. https://doi.org/10.1158/1078-0432.Ccr-17-0010.

64. Ianevski, A., Giri, A.K., and Aittokallio, T. (2022). SynergyFinder 3.0: an interactive analysis and consensus interpretation of multi-drug synergies across multiple samples. Nucleic Acids Res. *50*, W739–W743. https://doi.org/10.1093/nar/gkac382.

65. Heinz, S., Benner, C., Spann, N., Bertolino, E., Lin, Y.C., Laslo, P., Cheng, J.X., Murre, C., Singh, H., and Glass, C.K. (2010). Simple Combinations of Lineage-Determining Transcription Factors Prime cis-Regulatory Elements Required for Macrophage and B Cell Identities. Mol. Cell *38*, 576–589. https://doi.org/10.1016/j.molcel.2010.05.004.

66. Zhang, Y., Liu, T., Meyer, C.A., Eeckhoute, J., Johnson, D.S., Bernstein, B.E., Nusbaum, C., Myers, R.M., Brown, M., Li, W., and Liu, X.S. (2008). Model-based analysis of ChIP-Seq (MACS). Genome Biol. *9*, R137–R139. https://doi.org/10.1186/GB-2008-9-9-R137/FIGURES/3.

67. Yu, G., Wang, L.-G., and He, Q.-Y. (2015). ChIPseeker: an R/Bioconductor package for ChIP peak annotation, comparison and visualization. Bioinformatics *31*, 2382–2383. https://doi.org/10.1093/bioinformatics/btv145.

68. Thomas-Chollier, M., Herrmann, C., Defrance, M., Sand, O., Thieffry, D., and Van Helden, J. (2012). RSAT peak-motifs: motif analysis in full-size ChIP-seq datasets. Nucleic Acids Res. *40*, e31. https://doi.org/10.1093/nar/gkr1104.

69. Love, M.I., Huber, W., and Anders, S. (2014). Moderated estimation of fold change and dispersion for RNA-seq data with DESeq2. Genome Biol. *15*, 550. https://doi.org/10.1186/S13059-014-0550-8/FIGURES/9.

70. Benjamini, Y., and Hochberg, Y. (1995). Controlling the False Discovery Rate: A Practical and Powerful Approach to Multiple Testing. J. Roy. Stat. Soc. B *57*, 289–300. https://doi.org/10.1111/J.2517-6161.1995.TB02031.X.

71. Butler, A., Hoffman, P., Smibert, P., Papalexi, E., and Satija, R. (2018). Integrating single-cell transcriptomic data across different conditions, technologies, and species. Nat. Biotechnol. *36*, 411–420. https://doi.org/10.1038/nbt.4096.

72. Tsoi, J., Robert, L., Paraiso, K., Galvan, C., Sheu, K.M., Lay, J., Wong, D.J.L., Atefi, M., Shirazi, R., Wang, X., et al. (2018). Multi-stage Differentiation Defines Melanoma Subtypes with Differential Vulnerability to Drug-Induced Iron-Dependent Oxidative Stress. Cancer Cell *33*, 890–904.e5. https://doi.org/10.1016/j.ccell.2018.03.017.

STAR★METHODS

KEY RESOURCES TABLE

REAGENT or RESOURCE	SOURCE	IDENTIFIER
Antibodies		
ACTB	IGBMC house-made	N/A
ATM	Cell Signaling Technology	Cat# 2873; RRID:AB_2062659
AXL	Proteintech	Cat# 13196-1-AP; RRID:AB_10642006
BAHCC1	Thermo Fisher Scientific	Cat# PA5-54785; RRID:AB_2638459
BRG1	Abcam	Cat# ab110641; RRID:AB_10861578
FLAG	Sigma-Aldrich	Cat#F7425; RRID:AB_439687
GFP	Abcam	Cat#ab290; RRID:AB_2313768
H3K27ac	Abcam	Cat#ab4729; RRID:AB_2118291
HA	Abcam	Cat#ab9110; RRID:AB_307019
γH2AX	Sigma-Aldrich	Cat#05–636; RRID:AB_309864
IgG control	Abcam	Cat#ab171870; RRID:AB_2687657
c-JUN	Cell Signaling Technology	Cat# 9165 (also 9165T, 9165S, 9165L), RRID:AB_2130165
Ki67	Abcam	Cat# ab15580; RRID:AB_443209
LUCIFERASE	Santa Cruz Biotechnology	Cat# sc-57604; RRID:AB_629896
MITF	Cell Signaling Technology	Cat# 12590, RRID:AB_2616024
SOX9	Cell Signaling Technology	Cat# 82630; RRID:AB_2665492
SOX10	Cell Signaling Technology	Cat# 89356 (also 89356S); RRID:AB_2792980
VINCULIN	Sigma-Aldrich	Cat# V4505; RRID:AB_477617
Biological samples		
Histological sections of nevi and cutaneous melanoma samples	Prof. B. Cribier, head of the *Laboratoire d'histopathologie et d'immunopathologie cutanees*, Strasbourg CHU hospital	N/A
Histological sections primary uveal melanoma tumor sections	Nice CHU hospital.	Pandiani et al.[33]
Chemicals, peptides, and recombinant proteins		
CellTrace™ Violet Proliferation Kit	Fisher Scientific	C34557
Doxycycline	ENVIGO	TD.00502
Fugene6	Roche Diagnostics	1815075
Lipofectamine 2000	Fisher Scientific	11668027
Lipofectamine RNAiMAX	Fisher Scientific	13778030
NCS	Sigma Aldrich	N9162
SYBR Green	Roche Diagnostics	4887352001
Critical commercial assays		
Affinity Gel FLAG M2 conjugated beads	Sigma Aldrich	M8823
AnnexinV-APC	BD Biosciences	88-8007-72
CUT&Tag-IT™ Assay Kit	Active motif	#53165, #53160
Culturex® Basement Membrane Extract	R&D systems	3434-001-02
GentleMACS C-tubes	Miltenyibiotec	130-096-334
Human Tumor dissociation kit	Miltenyibiotec	130-095-929
LAB-TEK II chamber slides	Thermo Fisher Scientific	154461
Matrigel	Corning	356231
NucleoSpin RNA Plus kit	Macherey-Nagel	740990

(*Continued on next page*)

Continued

REAGENT or RESOURCE	SOURCE	IDENTIFIER
ProLong™ Gold antifade reagent	Invitrogen	P36930
Reverse Transcriptase Superscript IV	Life Technologies	18090050
Deposited data		
CUT&Tag	This paper	GSE205462
RNA-seq	This paper	GSE201702
RNA-seq	Scatolini et al.51	GSE12391
RNA-seq	Tsoi et al.[52]	GSE80829
RNA-seq	Badal et al.[51]	GSE98394
RNA-seq	Yan et al.[52]	GSE114445
RNA-seq	Kabbarah et al.[53]	GSE46517
RNA-seq	Xu et al.[54]	GSE8401
Experimental models: Cell lines		
All MM melanoma cells	Dr. G. Ghanem (Institute Jules Bordet, Brussels, Belgium) and J-C Marine (VIB-KU Leuven, Belgium)	Verfaillie et al.[16]
OMM1.3	Pandiani et al.[33]	N/A
OMM2.5	Pandiani et al.[33]	RRID:CVCL_C307
Hermes3A	Dr. C Bennett, University of London (UK)	RRID:CVCL_VS10
U-2 OS	ATCC	RRID:CVCL_0042
501mel HA-BAHCC1^{BAH}	This paper	N/A
501mel	Dr. C Goding, University of Oxford (UK)	RRID:CVCL_4633
HEK293T	ATCC	RRID:CVCL_0063
SKMEL-28	Dr. L Larue, Institut Curie) (France)	RRID:CVCL_0526
IGR37	Dr. C Goding, University of Oxford (UK)	RRID:CVCL_2075
Experimental models: Organisms/strains		
NOD.Cg-Prkdc^{scid} IL2rg^{tm1Wjl}/SzJ (NSG)	Jackson Laboratories	RRID:BCBC_4142
Oligonucleotides		
GR^{NEG}: TCATACTATATGACAG	This study	N/A
GR$^{\#1}$: AGATTGGCGGTAGGAA	This study	N/A
GR$^{\#2}$: TCCGTGGAATTTAGAT	This study	N/A
gRNA SE17q25$^{\#1}$: GGCACGAGGCGCATAGCTA	This study	N/A
gRNA SE17q25$^{\#2}$: TGCACGCCCCTCTTGTTCAG	This study	N/A
gRNA SE17q25$^{\#3}$: CTGATTTCTACCCTTCCGTG	This study	N/A
SI^{NEG}	ON-TARGETplus SMARTpool L-001830-10	Orizon Discovery
SI$^{\#1}$	ON-TARGETplus SMARTpool L-023331-02	Orizon Discovery
siMITF	ON-TARGETplus SMARTpool L-008674-00	Orizon Discovery
siSOX10	ON-TARGETplus SMARTpool L-017192-00	Orizon Discovery
Recombinant DNA		
pcDNA-FLAG	This study	N/A
pX629_dCas9_KRAB_mScarlet	This study	N/A
pCDNA-GFP	This study	N/A
pcDNA-GFP-SE17q25	This study	N/A
pcDNA-FLAG-BAHCC1^{TUDOR}	This study	N/A
pcDNA-FLAG-BAHCC1^{BAH}	This study	N/A
pLT3_shCTRL	This study	N/A
pLT3_sh4 (shBAHCC1)	This study	N/A

(*Continued on next page*)

Continued

REAGENT or RESOURCE	SOURCE	IDENTIFIER
pGL4.10Luc2	This study	N/A
pLenti6-GFP	This study	N/A
pLenti-TET-3HA-BAHCC1^{BAH}	This study	N/A
pLenti6-3HA-BAHCC1$^{BAH-TUDOR}$	This study	N/A
Software and algorithms		
FlowJo software	https://www.flowjo.com/solutions/flowjo/downloads	N/A
Seurat software package version 3.1.4	Butler et al.[55]	N/A
Fiji	https://imagej.net/software/fiji/downloads	N/A
DeepTool2	Ramírez et al.[56]	N/A
DiffBind v1.12.3	Ross-Innes et al.[26]	N/A
ROSE	Lovén et al.[23]	N/A
Homer v4.9.1	Heinz et al.[57]	N/A
ChIPseeker	Yu et al.[58]	N/A
Seq-MINER	Ye et al.[59]	N/A
Homer makeUCSCfile v4.9.1	Heinz et al.[57]	N/A
Cutadapt version 1.10	https://cutadapt.readthedocs.io/en/v1.10/	N/A
Bowtie v 2.2.8	Langmead et al.[60]	N/A
STAR version 2.5.3a	Dobin et al.[61]	N/A
Scope	https://scope.aertslab.org	N/A
Bioconductor package AUCell v 1.6.1	https://www.bioconductor.org/packages/release/bioc/html/AUCell.html	N/A
Deeptools multiBamSummary v2.5.0	Ramírez et al.[56]	N/A
Htseq-count version 0.6.1p1	https://htseq.readthedocs.io/en/master/history.html	N/A
Bioconductor package DESeq2 version 1.16.1	https://bioconductor.org/packages/release/bioc/html/DESeq2.html	N/A
Prism 9	https://www.graphpad.com/scientific-software/prism/	N/A
iRegulon plugin of Cytoscape	https://apps.cytoscape.org/apps/iregulon	N/A
Graeber Lab software	https://systems.crump.ucla.edu/	N/A
CCLE portal	https://sites.broadinstitute.org/ccle	N/A
Regulatory Sequence Analysis Tools (RSAT) web server	Thomas-Chollier et al.[62]	N/A
Other		
High-throughput imaging system CX7	Thermofisher	N/A
EVOS xl Core microscope	Thermofisher	N/A
IVIS imager	Perkin Elmer	N/A
Q800R3 sonicator	Qsonica	N/A
LightCycler 480	Roche	N/A
Illumina HiSeq 4000	Illumina	N/A
gentleMACS^{TM} Dissociator	Miltenyibiotec	N/A

RESOURCE AVAILABILITY

Lead contact

Further information and requests for resources and reagents should be directed to and will be fulfilled by the Lead Contact, Frédéric Coin (fredr@igbmc.fr).

Materials availability

Reagents generated in this study will be made available on request, but we may require a payment and/or a completed Materials Transfer Agreement if there is potential for commercial application.

Data and code availability

- Next generation sequencing raw and processed data have been deposited at GEO: Accession numbers of these data are listed in the key resources table
- This paper analyzes existing, publicly available data. These accession numbers for the datasets are listed in the key resources table
- This paper does not report original code
- Any additional information required to reanalyze the data reported in this paper is available from the lead contact upon request

EXPERIMENTAL MODEL AND STUDY PARTICIPANT DETAILS

Human sample collection

Information about human tumor samples is provided in Ext. Table S7. Nevi 1; male/62yo, Nevi 2; female/45yo, Tumor 1; male/50yo, Tumor 2; female/66yo, Tumor 3; male/70yo, Tumor A; female/84yo, Tumor B; male/69yo, Tumor C; male/84yo, Tumor D, male/65yo.

Tumors for cutaneous melanoma were obtained after written informed consent from the University of Strasbourg Medical facutly ethics board and good clinical practice. Tumors 1, 2 and 3 are identical to tumors 4, 5 and 6 described in.[63] Tumors A, B, C and D for uveal melanoma were obtained after written informed consent from the Nice CHU hospital. They are identical to tumor A, B, C and D described in.[33]

Cell culture

Patient-derived short-term cultures MM cells have been grown in HAM-F10 (Gibco, Invitrogen) supplemented with 10% Fetal Calf Serum (FCS) and penicillin-streptomycin. 501mel and SK-MEL-28 cells were grown in RPMI w/o HEPES (Gibco, Invitrogen) supplemented with 10% FCS and gentamycin and IGR37 and IGR39 were grown in RPMI w/o HEPES supplemented with 15% of FCS and gentamycin. Uveal melanoma cells OMM1.3 and OMM2.5 were cultured respectively in DMEM (4.5 g/L glucose) supplemented with 10% FCS, penicillin-streptomycin, Sodium Pyruvate, MEM essential vitamin mixture, NEAA mixture and HEPES, and RPMI w/o HEPES supplemented with 2gr/l glucose, 10% FCS and penicillin-streptomycin. U-2 OS cells were grown in DMEM/Ham-F10 (1:1) supplemented with 10% FCS and gentamicin. HEK293T cell were grown in DMEM (1 g/L glucose) supplemented with 10% FCS and penicillin-streptomycin. All cell lines were grown in 5% CO_2 at 37°C. Melanocyte cell line Hermes3A was grown in 10% CO_2 at 37°C in RPMI w/o HEPES supplemented with 10% FCS, penicillin-streptomycin, 200nM TPA (Sigma Aldrich), 200p.m. Cholera Toxin (Sigma Aldrich), 10 ng/mL hSCF (Life Technologies), 10nM EDN-1 (Sigma Aldrich) and 2mM Glutamine (Invitrogen). All cell lines used were mycoplasma negative.

501mel for *in vivo* studies were generated by transducing cells first with lentiviral vector pEIGW-SK II Luc-GFP (kindly provided by Dr. Iannis Aifantis) followed by a second transduction with MISSION shRNA lentiviral vectors shNTC (Millipore Sigma, SHC002), shBAHCC1$^{\#1}$ (Millipore Sigma, TRCN0000230988) and shBAHCC1$^{\#2}$ (Millipore Sigma, TRCN0000217993).[45]

501mel HA-BAHCC1^{BAH} were generated by transducing cells with lentiviral vectors pLenti-TET-3HA-BAHCC1^{BAH} and selected with 0.5ug/mL of puromycin.

Cells carrying a doxycycline-inducible system were treated with 1ug/mL of doxycycline for at least 24h.

GapmeRs or siRNAs were transfected in cells with Lipofectamine RNAiMAX following the manufacture instructions using an oligos final concentration of 25nM and cells were harvested 48h and/or 72h after transfection.

For CRISPRi experiments, 501mel cells were co-transfected with pX629_dCas9_KRAB_mScarlet (plasmid obtained from the IGBMC BioMol service) and pCDNA-GFP (gCTRL) or pcDNA-GFP-SE17q25 (gSE17q25) using Fugene6 following manufacture instructions. Afterward, double-positive GFP+/mScarlet+ cells were sorted with a FACSaria Fusion BD Biosciences Cell sorter and RNA extraction was performed 72h post sorting.

BAHCC1^{TUDOR} and BAHCC1^{BAH} were cloned into a pcDNA-FLAG vector. pcDNA-FLAG, pcDNA-FLAG-BAHCC1^{TUDOR}, pcDNA-FLAG-BAHCC1^{BAH}, pLenti6-GFP and pLenti6-3HA-BAHCC1$^{BAH-TUDOR}$ vectors were transiently transfected in HEK293T cells with Lipofectamine 2000 following the manufacture instructions.

Mouse xenograft studies

Animal experiments were performed in NYU Langone Health and were approved by the Institutional Animal Care and Use Committee (IACUC) under the protocol number IA16-00051. All experiments conform to the relevant regulatory standards.

Immunodeficient 6 weeks-old male mice NOD.Cg-Prkdc^{scid} IL2rg^{tm1Wjl}/SzJ (NSG) were purchased from Jackson Laboratories and maintained in the NYU Langone Health SBCAF germ-free animal facility. For primary tumor formation, 1 × 10^5 501mel cells were resuspended in 50μL of PBS +50μL of Corning Matrigel Matrix Basement Membrane (ref. 354234) and injected intradermally in the flank of the animal.

Primary tumor volume was measured every 3 days after becoming palpable using two-dimensional caliper (volume = (π/6) × length × wide^2) and animals were euthanized when tumors reached 1cm^3 volume.

For *in vivo* metastasis assay, 1 × 10^5 501mel cells were resuspended in 100μL of PBS mice and injected in the heart left ventricle of NSG mice through ultrasound imaging-guided injection. Metastasis burden was quantified once per week through luciferase injection followed by bioluminescence measurement with *In Vivo* Imaging System (IVIS) imager at the NYULH Preclinical Imaging Core. Animals were euthanized when the body weight reached a 20% decrease.

After euthanasia, mouse organs were collected and analyzed by *ex vivo* GFP fluorescence using a Zeiss AxioObserver microscope in the NYULH Microscopy Laboratory. Organs were then fixed in 10% Formalin for 72hrs followed by 72hrs in ethanol 70% before paraffin inclusion, sectioning, hematoxylin & eosin staining and imaging at the NYULH Experimental Pathology Research Laboratory.

METHOD DETAILS

Synergy assay

24 h after transfection with GAPMERs, 501mel or MM047 cells were seeded into 96-well plates at 5.000 cells/well. 24 h later, cells were incubated with combinations of increasing concentrations of the MEK inhibitor Trametinib or the PARP inhibitor Olaparib, for 72 h. Cell viabilities were assessed using PrestoBlue reagent (ThermoFisher) according to the manufacturer's instructions. The absorbance was measured with a Cell-Insight CX5 microplate reader. Synergy scoring was then determined using the SynergyFinder software (https://synergyfinder.fimm.fi) and by implementing the ZIP calculation method.[64]

Identification of SEs

H3K27ac ChIP-seq data from 12 different melanoma cell lines (MM001, MM011, MM031, MM034, MM057, MM074, MM047, MM087, MM099, MM118, SK-MEL-5, 501mel) and 3 melanocytes cell lines (NHEM1, NHEM2, Foreskin) were retrieved from GEO GSE60666, GSM958157 and GSE94488 and mapped to the Homo Sapiens genome (assembly hg19) using Bowtie v1.0.0 with default parameters except for "-p 3 -m 1 –strata –best –chunkmbs 128". Normalized BigWig files were generated using Homer makeUCSCfile v4.9.1[65] with the following parameter'-norm 20e6′ meaning that data were normalized to 20M reads. The genome was divided into bins of 10Kb long with Deeptools multiBamSummary v2.5.0.[57] The number of reads for each bin was computed for each sample. The following figure was made with Deeptools plotCorrelation and shows the pairwise correlation values (Spearman) for all samples of this project. Peaks were called using MACS2 with default parameters except for "-g hs -f BAM –broad –broad-cutoff 0.1". Peaks falling into ENCODE blacklisted regions ("An Integrated Encyclopedia of DNA Elements in the Human Genome" 2012–9AD) were removed. Peaks were annotated relative to genomic features using Homer v4.9.1 (annotations got extracted from gtf file downloaded from ensembl v75). ROSE was used to differentiate SEs from typical enhancers (detected from H3K27ac data). SEs were annotated relative to genomic features using Homer v4.9.1 (annotations got extracted from gtf file downloaded from ensembl v75). Finally, SEs were filtered according to their position relative to the one of SOX10 and MITF (ChIP-seq tracks in 501mel)[24,25] using the bioconductor package DiffBind v1.12.3.[56]

RNA FISH

Assays were performed following the manufacturer's instructions (https://acdbio.com/manual-assays-rnascope). For the detection of BAHCC1 and SOX10, cells and paraffin tissue sections were treated following the RNAScope manufacture protocol. Cells and tissue samples were counterstained with DAPI and visualized using confocal microscope Spinning disk Leica CSU W1. The sequences of the probes were not provided by the manufacture.

Protein extraction

For the production of whole cell extracts, cells were washed once with cold PBS, rinsed with a cell scraper, pelleted and resuspended in LSDB 0.5M buffer (0.5M KCl, 50mM Tris HCl pH 7.9, 20% Glycerol, 1% NP40, 1mM DTT, PIC). Afterward cells were fully disrupted with 3 cycles of heat shock in liquid nitrogen and 37°C water bath and centrifugated 15 min at 14,000rpm to pellet cell debris.

To obtain cytoplasmic and nuclear protein fractions, cells were first lysed in hypotonic buffer (10 mM Tris–HCl at pH 7.65, 1.5 mM $MgCl_2$, 10 mM KCl) and disrupted by Dounce homogenizer. The cytosolic fraction was separated from the pellet by centrifugation at 4°C. The nuclear soluble fraction was obtained by incubation of the pellet in high salt buffer (final NaCl concentration of 300 mM) and then separated by centrifugation at 4°C. To obtain the nuclear insoluble fraction (chromatin fraction), the remaining pellet was digested with micrococcal nuclease and sonicated.

Co-immunoprecipitation

Whole cell extract was prepared by resuspending cells in LSDB buffer (50mM Tris HCl pH 7.9, 20% Glycerol, 1% NP40, 1mM DTT, PIC) containing 150mM KCl, followed by sonication in Q800R3 sonicator. Between 250ug-1mg of protein extract was used to performed IP with 1-10μg of primary antibody overnight at 4°C on rotation. Following, 50ul of Dynabeads protein A/G were added to the samples for 2h at 4°C. In alternative, FLAG-tagged proteins were immunoprecipitated directly using Affinity Gel FLAG M2 conjugated beads. Beads were washed five times with TGEN buffer (20mM Tris-HCl pH 7.65, 3mM $MgCl_2$, 0.1mM EDTA, 10% glycerol, 0.01% NP-40, PIC) containing 150mM NaCl. Samples were loaded on NuPage gel to perform Western blot.

RNA extraction and qRT-PCR

Total RNA isolation was performed according to the manufacture protocol with NucleoSpin RNA Plus kit. RNA was retrotranscribed with Reverse Transcriptase Superscript IV and qPCR was performed with SYBR Green and monitored by LightCycler 480. Gene expression results were normalized according to four housekeeping genes (HMBS, TBP, UBC and RPL13a). Primers for qRT-PCR and ChIP-qPCR were designed using Primer-BLAST.

Immunofluorescence

Human tissue sections were deparaffinized and dehydrated with Histosol and dilutions of ethanol 100%, 90%, 70% and 30% and rehydrated with demineralized water. Subsequently sections were boiled in Sodium Citrate buffer (0.1M Citric acid, 0.1M Sodium citrate) for 15min to unmask antigens. In parallel, 2D culture cells were grown on LAB-TEK II chamber slides and fixed with 4% formaldehyde or 100% methanol. Afterward, both tissues and cells were permeabilized and saturated in blocking buffer (1% BSA, PBS, 0.3% Triton X-100). Primary antibodies were diluted in blocking buffer and incubate ON at 4°C in wet chamber. Secondary antibody staining was carried out in blocking buffer for 1h and 30 min at room temperature. Nuclei were marked with DAPI and slides were mounted with ProLong Gold antifade reagent before microscope image acquisition.

For γH2AX foci quantification, transfected or naive cells were plated in 96 well plates OptiPlates-96 and eventually treated with NCS (150nM) for 1h at 37°C followed by 1h, 8h or 24h of recovery in complete medium. Afterward, cells were labeled for γH2AX following a classic immunofluorescence protocol. Image acquisition was done using high-throughput imaging system CX7 using 20X objective (50 fields per well). Image segmentation was done with HCS studio. Nuclei were identified using DAPI staining and γH2AX foci were identified within nuclei mask. Foci number and intensity were quantified automatically.

Cell proliferation assay

To measure cell proliferation, cells were incubated first with CellTrace Violet according to the manufacture instructions and analyzed by flow cytometry using a FORTESSA BD Biosciences Cytofluorometer. Data were analyzed with FlowJo software. To define slow proliferating cells, we considered that they represented the 30% of cells with the highest concentration of BV421 in the control treatment. We then calculated the % of cells that had a concentration greater than or equal to this value after treatment.

Cell death assay

To measure cell death, cells were rinsed and incubated 15min with AnnexinV-APC after treatment and analyzed by flow cytometry on a FORTESSA BD Biosciences Cytofluorometer. Data were analyzed with FlowJo software.

Cell density assay

Briefly, following transfection, between 5.10^4 to 1.10^5 cells were grown in 6 wells plate for up to 1 week. Afterward cells were fixed for 10min with 4% Formaldehyde solution, washed once with PBS and stained with Crystal Violet solution 0.2% for 15 min at room temperature. The wells were finally washed twice with deionized water, air dried, scanned and analyzed with Fiji considering the area occupancy of the cells.[26]

Cell invasion assay

Briefly, between 1 and 2.10^5 cells were seeded inside a Boyden Chamber insert covered with Serum free media and 4% Matrigel. The inserts were placed in 24 wells plate filled with complete medium. After 12-24h, the inserts were fixed with 4% Formaldehyde solution for 10min, gently cleaned inside with a cotton stick and stained for 15 min at room temperature with a Crystal Violet solution 0.2%. Afterward the inserts were washed twice in deionized water, air dried and photos were collected using an EVOS xl Core microscope. The pictures were analyzed with Fiji considering the area occupancy of the cells.

CUT&Tag and deep sequencing

Assays were performed following the manufacturer's instructions (https://www.activemotif.com/catalog/1318/cut-tag-it-kit). Briefly, 5.10^5 cells per condition were used. The cells were washed 2 time before the binding on Concavalin A beads and then incubated overnight with BAHCC1 ($BAHCC1^{WT}$) or HA ($BAHCC1^{TUDOR-BAH}$) primary antibodies at the recommended dilution (1:50) or without antibody (negative control). The next day the corresponding secondary antibody, a guinea pig Anti-rabbit antibody was used following a 1:100 dilution in digitonin buffer and incubated at room temperature for 1h. The CUT&Tag-IT Assembled pA-Tn5 Transposomes were incubated for 1h at room temperature before tagmentation. Cells were resuspended in Tagmentation buffer and incubated at 37°C for 1h, then the Tagmentation process was stopped by addition of EDTA and SDS. Protein digestion was performed by the addition of 80ug/mL of proteinase K and incubated at 55°C for 60min. DNA was retrieved on DNA purification columns provided by the manufacturer. Library preparation and PCR amplification were done using the Kit primers and purified by 2 successive washes with SPRI beads. Samples were subjected to paired-end sequencing by the IGBMC GenomEast platform on Illumina HiSeq 4000 instrument.

Deep sequencing analysis

ChIP-seq data for BRG1,[25] H3K27ac and ATAC-seq[8] and CUT&Tag-seq for BAHCC1 (this work) were analyzed as follows.[26] After reads mapping onto hg19 human genome, peak calling was performed using MACS2 according to specific negative control inputs.[66]

Peak annotation was carried out using HOMER[65] and ChIPseeker.[67] Peak genome distribution and correlation between BAHCC1 and BRG1, H3K27ac and ATAC was performed using deepTool2. Peak enrichment for BRG1, H3K27ac, ATAC and BAHCC1 was done using seq-MINER. Top 500 macs peaks summits for BAHCC1 alone or co-bound by BAHCC1 and BRG1 (identified with seq-MINER)[58] were subsequently extended of 100bp upstream and downstream using "bedtools slop" followed by extraction of FASTA format sequences with "bedtools getfasta". DNA binding motif analysis was carried out with Simple Enrichment Analysis (SEA)[59] and by the pipeline "peak-motifs" available online as part of the Regulatory Sequence Analysis Tools (RSAT)[68] using +/− 400bp around the center to cut peak sequences and the non-redundant vertebrate Jaspar core database for motif comparison.

Bulk RNA-seq analysis

Reads were preprocessed to remove adapter and low-quality sequences (Phred quality score below 20). After this preprocessing, reads shorter than 40 bases were discarded for further analysis. These preprocessing steps were performed using cutadapt version 1.10. Reads were mapped to rRNA sequences using bowtie version 2.2.8[62] and reads mapping to rRNA sequences were removed for further analysis. Reads were mapped onto the hg19 assembly of Homo sapiens genome using STAR version 2.5.3a.[60] Gene expression quantification was performed from uniquely aligned reads using htseq-count version 0.6.1p1, with annotations from Ensembl version 75 and "union" mode. Only non-ambiguously assigned reads have been retained for further analyses. Read counts have been normalized across samples with the median-of-ratios method proposed by Anders and Huber[61] to make these counts comparable between samples. Comparisons of interest were performed using the Wald test for differential expression proposed by Love[69] and implemented in the Bioconductor package DESeq2 version 1.16.1. Genes with high Cook's distance were filtered out and independent filtering based on the mean of normalized counts was performed. P-values were adjusted for multiple testing using the Benjamini and Hochberg method.[70] iRegulon plugin of Cytoscape was used to analyze the co-deregulated genes between iBAHCC1 and iBRG1.

Single cell data analysis

Expression matrix with row reads counts for the single cell experiment was retrieved from GEO GSE116237, GSE115978, GSE151091, GSE138665, GSE185386 and GSE113502 datasets. Then, data were normalized and clustered using the Seurat software package version 3.1.4 in R version 3.6.1.[71] Data were filtered and only genes detected in at least 3 cells and cells with at least 350 detected genes were kept for further analysis. Expression of 26,661 transcripts in single cells was quantified. To cluster cells, read counts were normalized using the method "LogNormalize" of the Seurat function NormalizeData. It divides gene expression counts by the total expression, multiplies this by a scale factor (10,000 was used), and log-transforms the result. Then, 2000 variable features were selected with the variance stabilizing transformation method using the Seurat function FindVariableGenes with default parameters. Integrated expression matrices were scaled (linear transformation) followed by principal component analysis (PCA) for linear dimensional reduction. The 20 principal components (PCs) were used to cluster the cells with a resolution of 0.5 and as input to tSNE to visualize the dataset in two dimensions. The Bioconductor package AUCell v 1.6.1 was used to assess whether some cells from the different datasets were enriched in gene sets of interest.

Other publicly available datasets used in this work

BAHCC1 RNA expression was quantified in available datasets including GEO GSE12391,[55] GSE80829,[72] GSE98394,[51] GSE114445,[52] GSE46517,[53] GSE8401[54] and in the CCLE portal. TCGA and GTEx data were obtained through UCSC Xena browser, cBioPortal and Gene Expression Profiling Interactive Analysis 2 (GEPIA2). PCA profile of TCGA and melanoma cell lines according to their phenotypic profile was obtained from the Graeber Lab software.

QUANTIFICATION AND STATISTICAL ANALYSIS

Statistical analysis was mostly performed using Prism 9. Briefly, for absolute quantification comparison, Student's t-test and ordinary one-way ANOVA unpaired were used; paired test was used for relative quantification comparisons. Grouped sample analysis was carried out through two-way ANOVA test. Kaplan-Meier survival curves were analyzed using Mantel-Cox test. For correlation analysis, Spearman analysis was performed together with linear regression curve fit. Statistical analysis on RNA-seq and ChIP-seq is listed in their dedicated sections. For Venn diagram statistic, hypergeometric test was performed using Nemates software (nemates.org). p values are represented as ns ($p > 0.05$), * ($p < 0.05$), ** ($p < 0.01$), *** ($p < 0.005$) and **** ($p < 0.001$).